# Generalized Matched Filter for Radar Range Sidelobe Suppression: An Oblique Projection Approach

Yalong Wang, *Graduate Student Member, IEEE*, Xuejing Zhang, *Member, IEEE*, Jinyang He, Jun Li, and Zishu He, *Senior Member, IEEE*

***Abstract*—The standard matched filter (MF) inherently causes small targets to be masked by range sidelobes of nearby large targets, posing a fundamental challenge for precise range profile extraction. In this paper, we develop a generalized matched filter (GMF) using oblique projection to suppress range sidelobes. Compared to the standard MF, the proposed GMF can flexibly create a specified zero correlation zone (ZCZ) within the specified lag region of interest, while preserving the peak correlation level without loss. Given a transmit sequence, the GMF is presented as a closed form. Moreover, it can be applied to various transmit sequences and exhibits high range resolution. The GMF can be well-designed offline and then implemented online for pulse compression. It provides greater efficiency than existing online signal processing methods. In this paper, we conduct a comprehensive performance analysis of GMF. The distinctions and connections between GMF and MF are presented. In addition, we explore the cost introduced by high range resolution within the GMF framework and present an enhanced GMF by optimizing the transmit sequence. Also, several extended applications of the GMF are discussed. Representative simulation results confirm the effectiveness and superiority of the proposed method.**

***Index Terms*—Generalized matched filter, oblique projection, output signal-to-noise ratio loss, range resolution, zero correlation zone.**

## I. Introduction

In active sensing systems, such as the radar system, precise target range profile extraction under the noise background is a fundamental requirement, and the output signal-to-noise ratio (SNR) is a primary metric for evaluating target detectability [1], [2], [3]. For a point target in the presence of white noise, it is well known that the matched filter (MF) maximizes the output SNR, enhancing the target detectability in a certain sense [1]. However, in multitarget scenarios, the range profiles of small targets are usually masked by nearby large targets due to the limitations of standard matched filtering.

To overcome the range sidelobe masking problem, the first strategy is to conduct dedicated signal processing methods, and various mismatched filter approaches have been extended for pulse compression (PC). For example, the least squares (LS) method decouples neighboring range cells to attain a satisfactory range profile estimation within the given processing window [4], [5]. However, when there are strong targets outside the processing window, the range profile estimation performance of the LS method deteriorates significantly. In addition, various adaptive range processing methods are developed for range profile extraction. For example, the CLEAN algorithm sequentially subtracts the estimated range sidelobe levels introduced by large targets [6], [7]. The CLEAN algorithm can suppress the range sidelobes of large targets to some extent, but it still encounters difficulties in accurately extracting the range profiles of masked small targets. The adaptive pulse compression (APC) approach employs the current estimate of the measured range profile amplitudes to yield a reiteratively adaptive minimum mean square error (MMSE) filter for each range cell [8]. However, constructing individualized MMSE filters for each range cell imposes a huge computational burden and is unsuitable for real-time applications. Therefore, several computationally efficient variants are developed for the APC method [9], [10]. Besides, the authors of [11] propose a robust APC method for range sidelobe suppression. It should be noted that the methods demonstrated in [11] are almost for linear frequency modulation (LFM) signals and also require a certain calculation cost.

As we know, the correlation of the MF for a given sequence is essentially determined by its auto-correlation. On this basis, the second strategy involves designing sequences to suppress range sidelobes[1]. Ideally, the aperiodic auto-correlation function (AAF) is expected to take the form of the Kronecker delta function. However, due to physical limitations, achieving an

Received 3 April 2025; revised 5 August 2025 and 1 October 2025; accepted 27 October 2025. Date of publication 29 October 2025; date of current version 12 December 2025. This work was supported in part by the National Natural Science Foundation of China under Grant 62371093, Grant 62101101, Grant 62231006, and Grant 62031007, in part by Sichuan Science and Technology Program under Grant 2024NSFSC1433, and in part by Peng Cheng Shang Xue Education Fund under Grant XY2021602. The associate editor coordinating the review of this article and approving it for publication was Yuan Shen. *(Corresponding author: Xuejing Zhang.)*

The authors are with the School of Information and Communication Engineering, University of Electronic Science and Technology of China, Chengdu 611731, China (e-mail: wang_yal@163.com; zhangxuejing@uestc.edu.cn; jinyanghe@126.com; lijunsc@uestc.edu.cn; zshe@uestc.edu.cn).

Digital Object Identifier 10.1109/TSP.2025.3626860

[1]When discussing the correlation sidelobe, usually only the inherent characteristics of the transmit sequence are analyzed without considering factors such as noise. The range sidelobe, on the other hand, reflects the output response of the echo signal (the transmit sequence has been delayed, attenuated, and superimposed with noise components, etc) after filtering.

ideal AAF is impossible. Initially, lots of significant research focused on the design of binary and polyphase sequences. For instance, the well-known binary Barker sequence achieves a peak sidelobe level (PSL) no greater than 1, but its sequence length is limited to a maximum of 13 [12]. To this end, various polyphase Barker sequences are developed to enlarge the sequence length, though the extension remains finite [13], [14]. Besides, pulse-to-pulse sequence agility based on Golay complementary pairs can completely eliminate auto-correlation sidelobe levels [15], [16], [17]. However, the complementary property degrades in the presence of intrapulse Doppler shift, resulting in increased auto-correlation sidelobe levels.

With advancements in direct digital synthesis technology, the design of arbitrary phase sequences has been developed, typically leveraging optimization theory to minimize the integrated sidelobe level (ISL) or PSL [18], [19], [20], [21], [22], [23]. In certain applications, the zero correlation zone (ZCZ), which maintains ideal correlation properties only within a finite zone of lags, may be sufficient instead of requiring an AAF such as the Kronecker delta function [24]. For example, Stoica et al. introduce a weighted cyclic algorithm to minimize an "almost equivalent" criterion instead of directly minimizing the weighted ISL (WISL) metric [18]. Song et al. consider directly minimizing the original WISL metric by employing the majorization-minimization framework [25]. Furthermore, various algorithms such as phase gradient descent [26], alternating projection [27], pattern search [28], and alternating direction method of multipliers [29] have been developed for ZCZ sequence design. As demonstrated in [30], the ISL metric has an exact lower bound due to the matched receive filter constraint. To overcome this limitation, designing both the transmit sequence and receive filter could further suppress the correlation sidelobe level compared to its matched counterpart [31]. Transceiver design methods primarily fall into two categories: designing a receive filter based on a given transmit sequence [32], [33], [34] and jointly designing both the transmit sequence and receive filter [35], [36], [37], [38], [39], [40], [41], [42]. Accordingly, various transceiver design methods have been further developed for ZCZ [37], [38], [39], [40], [41], [42], [43]. It is important to note that mismatched filters result in a loss of peak correlation level. Consequently, the trade-off between the peak correlation level and sidelobe level remains a critical consideration.

In this paper, we present a generalized matched filter (GMF) framework for range sidelobe suppression, leveraging oblique projection. Specifically, the GMF is constructed with the transmit sequence and corresponding oblique projector. Compared to the standard MF, the proposed GMF can flexibly create a specified ZCZ within the specified lag region of interest, while preserving the peak correlation level without loss. Given a transmit sequence, the GMF is presented as a closed form. Moreover, it can be applied to various transmit sequences and exhibits high range resolution. In the absence of a prescribed lag region of interest, the GMF simplifies to the MF. We analyze the output SNR performance of the proposed GMF under white noise assumption. With the GMF framework, it is shown that the undesired output levels can be further suppressed by minimizing the filter energy. This further leads to a novel design metric for transmit sequence, which is formally equivalent to the output SNR loss. In addition, we explore the cost introduced by high range resolution within the GMF framework and present an enhanced GMF by optimizing the transmit sequence. Also, several extended applications of the GMF are discussed. The main contributions are summarized as follows:

1) We design a GMF framework for the range profile masking problem using the transmit sequence and the corresponding oblique projector. Under a specified transmit sequence, the GMF is derived in closed form and is compatible with various transmit sequences. The GMF can be well-designed offline and then implemented online for PC. It provides greater efficiency than existing online signal processing methods.
2) The derived GMF operates exclusively at the receiving end, providing high flexibility in practical applications. It can achieve high range resolution, establish a user-defined ZCZ while preserving the peak correlation level without loss. Additionally, its ZCZ performs better than existing sequence design methods.
3) We conduct a comprehensive performance analysis of GMF and derive a novel metric for sequence design. We reveal the cost of achieving high range resolution within the GMF framework. Moreover, an enhanced GMF framework is presented to control undesired output levels and achieve a negligible output SNR loss.

The rest of this paper is organized as follows. Section II introduces the range profile masking and sequence correlation problem. Section III analyzes the proposed generalized matched filter in detail. Section IV discusses the extension of proposed method in different scenarios and applications. Section V shows numerical results to demonstrate the superiority of the proposed method. Section VI concludes this paper.

*Notations:* In this paper, we use lightface for scalar $a$, lower case boldface for vector $\mathbf{a}$, and upper case for matrix $\mathbf{A}$. $\mathbf{A}^{-1}$ denotes the inverse of matrix $\mathbf{A}$. $\mathbf{A}_{n,:}$ represents the $n$th row vector of matrix $\mathbf{A}$. Double line body $\mathbb{C}$ means the complex numbers domain. $(\cdot)^T$, $(\cdot)^H$, $\otimes$, and $\mathbb{E}\{\cdot\}$ denote the transpose, conjugate transpose, Kronecker product, and statistical expectation operators, respectively. $\mathrm{Diag}\{\cdot\}$ stands for the diagonal matrix with diagonal elements equal to the input entries. $\mathbf{I}_{N\times N}$ and $\mathbf{0}_{N\times N}$ are the $N\times N$-dimensional identity matrix and zero matrix, respectively. $\mathbf{1}_N$ is the $N$-dimensional all-ones vector. $|\cdot|$ is the absolute value of a scalar or the determinant of a matrix. $\|\cdot\|_2$ denotes the $l_2$ norm. $\mathcal{R}(\cdot)$ returns the column space of the input matrix. $\mathcal{R}^{\perp}(\cdot)$ is the orthogonal complementary space of $\mathcal{R}(\cdot)$. $\propto$ means that the quantities on its both sides are directly proportional. $\lfloor\cdot\rfloor$ denotes the floor operation.

## II. Preliminaries

### A. Oblique Projection

The projection matrix (or projector) that is not orthogonal is referred to as an oblique projector. Let full column rank matrix $\mathbf{M}=[\mathbf{M}_1,\mathbf{M}_2]\in\mathbb{C}^{M\times(M_1+M_2)}$, where $\mathbf{M}_1\in\mathbb{C}^{M\times M_1}$ and $\mathbf{M}_2\in\mathbb{C}^{M\times M_2}$. Denote by $\mathbf{E}_{\mathbf{M}_1|\mathbf{M}_2}\in\mathbb{C}^{M\times M}$ the oblique

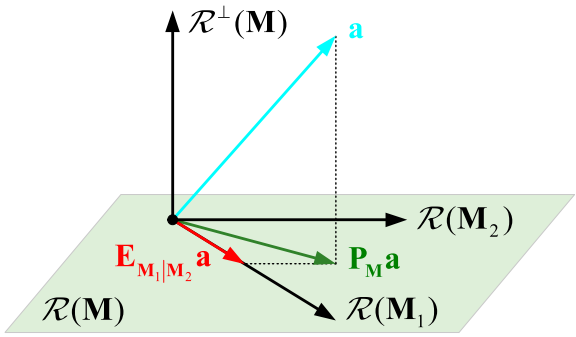


Fig. 1. Illustration of the oblique projector.

projector, which projects vectors onto $\mathcal{R}(\mathbf{M}_1)$ along the direction parallel to $\mathcal{R}(\mathbf{M}_2)$, as illustrated in Fig. 1, can be mathematically expressed as [44], [45]:

$$\begin{aligned}\mathbf{E}_{\mathbf{M}_1|\mathbf{M}_2} &= [\mathbf{M}_1, \mathbf{0}_{M\times M_2}](\mathbf{M}^H\mathbf{M})^{-1}\mathbf{M}^H \\ &= \mathbf{M}_1(\mathbf{M}_1^H\mathbf{P}_{\mathbf{M}_2}^{\perp}\mathbf{M}_1)^{-1}\mathbf{M}_1^H\mathbf{P}_{\mathbf{M}_2}^{\perp} \end{aligned} \tag{1}$$

where $\mathbf{P}_{\mathbf{M}_2}^{\perp}$ denotes the orthogonal projector onto $\mathcal{R}^{\perp}(\mathbf{M}_2)$, which can be expressed as

$$\mathbf{P}_{\mathbf{M}_2}^{\perp} = \mathbf{I}_{M\times M} - \mathbf{P}_{\mathbf{M}_2} = \mathbf{I}_{M\times M} - \mathbf{M}_2(\mathbf{M}_2^H\mathbf{M}_2)^{-1}\mathbf{M}_2^H$$

and $\mathbf{P}_{\mathbf{M}_2} = \mathbf{M}_2(\mathbf{M}_2^H\mathbf{M}_2)^{-1}\mathbf{M}_2^H$ is the orthogonal projector onto $\mathcal{R}(\mathbf{M}_2)$. It is easily verified that

$$\mathbf{E}_{\mathbf{M}_1|\mathbf{M}_2}\mathbf{M}_1 = \mathbf{M}_1,\ \mathbf{E}_{\mathbf{M}_1|\mathbf{M}_2}\mathbf{M}_2 = \mathbf{0}_{M\times M_2} \tag{2}$$

and $\mathbf{E}_{\mathbf{M}_1|\mathbf{M}_2}$ is idempotent but not Hermitian symmetric.

In fact, when $\mathbf{M} = [\mathbf{M}_1, \mathbf{M}_2]$ is not a full column rank matrix, the oblique projector $\mathbf{E}_{\mathbf{M}_1|\mathbf{M}_2}$ can also be effectively constructed, utilizing the principal left singular vector matrices $\mathbf{N}_1 \in \mathbb{C}^{M\times N_1}$ and $\mathbf{N}_2 \in \mathbb{C}^{M\times N_2}$ of $\mathbf{M}_1$ and $\mathbf{M}_2$, respectively, given by:

$$\mathbf{P}_{\mathbf{M}_2}^{\perp} = \mathbf{I}_{M\times M} - \mathbf{N}_2(\mathbf{N}_2^H\mathbf{N}_2)^{-1}\mathbf{N}_2^H \tag{3a}$$

$$\mathbf{E}_{\mathbf{M}_1|\mathbf{M}_2} = \mathbf{N}_1(\mathbf{N}_1^H\mathbf{P}_{\mathbf{M}_2}^{\perp}\mathbf{N}_1)^{-1}\mathbf{N}_1^H\mathbf{P}_{\mathbf{M}_2}^{\perp}. \tag{3b}$$

Under this setting, the prerequisite for (2) to hold is that matrix $[\mathbf{N}_1, \mathbf{N}_2]$ has a full column rank.

### B. The Range Profile Masking Problem

For the sake of illustration, we consider a length-$L$ complex valued transmit sequence $\mathbf{s} \in \mathbb{C}^L$:

$$\mathbf{s} = [s(1), \cdots, s(l), \cdots, s(L)]^T,\ l = 1, 2, \cdots, L \tag{4}$$

where $\forall l, s(l) \neq 0$. The length-$L$ received digital baseband signal $\mathbf{y}(n) \in \mathbb{C}^L$ of $n$th range cell can be expressed as [8]:

$$\mathbf{y}(n) = \mathbf{Z}(n)\mathbf{s} + \mathbf{n}(n) \tag{5}$$

where the intrapulse Doppler effect is negligible, and

$$\mathbf{Z}(n) = \begin{bmatrix} z(n) & z(n+1) & \cdots & z(n+L-1) \\ z(n-1) & z(n) & \cdots & z(n+L-2) \\ \vdots & \vdots & \ddots & \vdots \\ z(n-L+1) & z(n-L+2) & \cdots & z(n) \end{bmatrix}$$

denotes the target range profile impulse response matrix. $\mathbf{n}(n)$ is the white noise vector. By conducting the matched filtering using $\mathbf{s}$, the MF output of (5) is given by:

$$y_{\mathrm{MF}}(n) = \mathbf{s}^H\mathbf{Z}(n)\mathbf{s} + \mathbf{s}^H\mathbf{n}(n). \tag{6}$$

From (5) and (6), for the case of a solitary point target, $\mathbf{Z}(n)$ simplifies to $\mathrm{Diag}\{z(n), z(n), \cdots, z(n)\} \in \mathbb{C}^{L\times L}$, and the MF output reduces to $z(n)\mathbf{s}^H\mathbf{s} + \mathbf{s}^H\mathbf{n}(n)$. In this case, the MF is optimal and maximizes the output SNR. However, in the case of multitarget, if any off-diagonal elements of $\mathbf{Z}(n)$ are large relative to $z(n)$, the MF will mask the true value of $z(n)$, resulting in the range profile masking problem.

Discarding the term $\mathbf{s}^H\mathbf{n}(n)$ from (6), the MF output term $\mathbf{s}^H\mathbf{Z}(n)\mathbf{s}$ can be rewritten as:

$$\begin{aligned}\mathbf{s}^H\mathbf{Z}(n)\mathbf{s} &\triangleq z(n)\sum_{l=1}^{L}|s(l)|^2 \\ &\quad + \sum_{k=-L+1,k\neq 0}^{L-1} z(n-k)\sum_{l=1}^{L}s(l)s^*(l-k)\end{aligned} \tag{7}$$

where $k$ represents the lag index. From (7), we can see that even if the off-diagonal element $z(n-k)$ is large relative to $z(n)$, when $\left|\sum_{l=1}^{L}s(l)s^*(l-k)\right| \to 0, k \neq 0$ (i.e., low auto-correlation sidelobes of the transmit sequence $\mathbf{s}$), the range profile masking problem can also be effectively addressed. For the sake of illustration, let $\chi_{\mathbf{s},\mathbf{s}}(k)$ represent the AAF of $\mathbf{s}$:

$$\chi_{\mathbf{s},\mathbf{s}}(k) = \sum_{l=1}^{L} s(l)\, s^*(l-k),\ k = -L+1, \cdots, L-1. \tag{8}$$

To simplify the expression of (8), we introduce the aperiodic shifting matrix $\mathbf{J}_k \in \mathbb{C}^{L\times L}, k = -L+1, -L+2, \cdots, L-1$, with the $(i,j)$th element $[\mathbf{J}_k]_{i,j}$ in $\mathbf{J}_k$ defined as follows:

$$[\mathbf{J}_k]_{i,j} = \begin{cases} 1, & if\ i-j+k=0 \\ 0 & if\ i-j+k\neq 0 \end{cases}$$
$$(i,j) \in \{1, 2, \cdots, L\}^2. \tag{9}$$

Then the AAF $\chi_{\mathbf{s},\mathbf{s}}(k)$ in (8) can be recast as:

$$\chi_{\mathbf{s},\mathbf{s}}(k) = \mathbf{s}^H\mathbf{J}_k\mathbf{s},\ k = -L+1, -L+2, \cdots, L-1. \tag{10}$$

When $k=0$, $\mathbf{J}_0 = \mathbf{I}_{L\times L}$, the peak level of AAF appears and $\chi_{\mathbf{s},\mathbf{s}}(0) = \mathbf{s}^H\mathbf{s}$. When $k \neq 0$, $\chi_{\mathbf{s},\mathbf{s}}(k)$ is the auto-correlation sidelobe level of transmit sequence $\mathbf{s}$.

To overcome the range profile masking problem, a generalized matched filter is proposed next, by leveraging the transmit sequence and corresponding oblique projector.

## III. Proposed Generalized Matched Filter

In this section, we first derive the GMF in a closed-form expression and analyze the effectiveness of the oblique projector within the proposed GMF framework. Then, we examine the performance of the GMF in terms of zero correlation, range resolution, and output SNR. On this basis, we put forward the design strategy for enhanced GMF and extended GMF. In addition, we briefly outline the relationship between the proposed GMF and existing sequence design methods. Finally, we discuss its complexity.

### A. Design Framework of GMF

Building upon the preceding discussion, it is evident that the auto-correlation sidelobes generated by the MF are the primary cause of the range sidelobe. To this end, we attempt to design a filter that can achieve a zero correlation sidelobe between the designed filter and transmit sequence for range sidelobe suppression. By inserting an identity matrix $\mathbf{I}_{L\times L}$, the AAF $\chi_{\mathbf{s},\mathbf{s}}(k)$ in (8) can be further reformulated as follows:

$$\chi_{\mathbf{s},\mathbf{s}}(k)=\mathbf{s}^H\mathbf{I}_{L\times L}\mathbf{J}_k\mathbf{s},\ k=-L+1,-L+2,\cdots,L-1. \tag{11}$$

To suppress the correlation sidelobes while preserving the peak level, we propose constructing a "projector" instead of the identity matrix $\mathbf{I}_{L\times L}$ in (11). This "projector" is designed to project $\mathbf{J}_k\mathbf{s}$ ($k\neq 0$) onto the zero vector while simultaneously maintaining $\mathbf{J}_k\mathbf{s}$ ($k=0$) without distortion, thereby achieving zero correlation sidelobes and ensuring the peak correlation level without loss. To achieve this, we leverage the properties of oblique projection as demonstrated in Section II-A to construct an oblique projector $\mathbf{E}_{\mathbf{s}|\widetilde{\mathbf{A}}}$, which substitutes $\mathbf{I}_{L\times L}$ in (11), where

$$\widetilde{\mathbf{A}}=[\mathbf{J}_{-L+1}\mathbf{s},\cdots,\mathbf{J}_{-1}\mathbf{s},\mathbf{J}_1\mathbf{s},\cdots,\mathbf{J}_{L-1}\mathbf{s}]\in\mathbb{C}^{L\times(2L-2)}.$$

Let $\Omega_s=\{\pm1,\pm2,\cdots,\pm(L-1)\}$ represents the set of all correlation sidelobe lags. The designed oblique projector $\mathbf{E}_{\mathbf{s}|\widetilde{\mathbf{A}}}$ is expected to yield the following properties:

$$\mathbf{E}_{\mathbf{s}|\widetilde{\mathbf{A}}}\mathbf{J}_k\mathbf{s}=\mathbf{s},\quad k=0 \tag{12a}$$

$$\mathbf{E}_{\mathbf{s}|\widetilde{\mathbf{A}}}\mathbf{J}_k\mathbf{s}=\mathbf{0}_L,\ k\in\Omega_s. \tag{12b}$$

From Section II-A, it is important to note that the prerequisite for (12) to hold is that $\mathbf{s}\notin\mathcal{R}(\widetilde{\mathbf{A}})$. However, due to some practical limitations on the transmit sequence, it is difficult to satisfy $\mathbf{s}\notin\mathcal{R}(\widetilde{\mathbf{A}})$. To this end, a compromise solution is to suppress sidelobes at some lags of interest, i.e., select $L_A$ column vectors from $\widetilde{\mathbf{A}}$ to construct matrix $\mathbf{A}\in\mathbb{C}^{L\times L_A}, 0\leq L_A<2L-2$. Then, we need to ensure that $\mathbf{s}\notin\mathcal{R}(\mathbf{A})$, in other words,

$$\|\mathbf{P}_{\mathbf{A}}\mathbf{s}\|_2^2<\|\mathbf{s}\|_2^2 \tag{13}$$

necessarily holds. On this basis, we can leverage the modified oblique projector $\mathbf{E}_{\mathbf{s}|\mathbf{A}}$ instead of $\mathbf{E}_{\mathbf{s}|\widetilde{\mathbf{A}}}$, which has the following properties:

$$\mathbf{E}_{\mathbf{s}|\mathbf{A}}\mathbf{s}=\mathbf{s},\ \mathbf{E}_{\mathbf{s}|\mathbf{A}}\mathbf{A}=\mathbf{0}_{L\times L_A}. \tag{14}$$

It should be noted that the prerequisite for (14) to hold is that $\mathbf{s}\notin\mathcal{R}(\mathbf{A})$, regardless of whether $\mathbf{A}$ has a full column rank. This is because the oblique projector $\mathbf{E}_{\mathbf{s}|\mathbf{A}}$ can be effectively constructed using $\mathbf{s}$ and the principal left singular vector matrix $\mathbf{A}_{\text{SVD}}$ of $\mathbf{A}$, as demonstrated in (3). Thereby, $\mathbf{P}_{\mathbf{A}}$ in $\mathbf{E}_{\mathbf{s}|\mathbf{A}}$ can be computed by $\mathbf{P}_{\mathbf{A}}=\mathbf{A}_{\text{SVD}}(\mathbf{A}_{\text{SVD}}^H\mathbf{A}_{\text{SVD}})^{-1}\mathbf{A}_{\text{SVD}}^H$.

For clarity, denote $\Omega_s^{\|}$ and $\Omega_s^{\perp}$ the sets of interested and uninterested lags, respectively. The aforementioned sets satisfy the following relationship:

$$\Omega_s^{\|}\cup\Omega_s^{\perp}=\Omega_s,\ \Omega_s^{\|}\cap\Omega_s^{\perp}=\varnothing \tag{15}$$

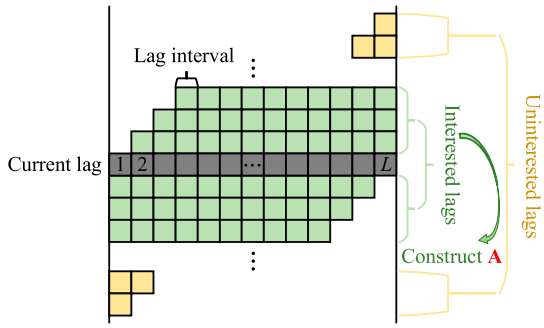


Fig. 2. Schematic diagram of the construction method of $\mathbf{A}$.

where $\Omega_s^{\|}$ and $\Omega_s^{\perp}$ can be designed with specific requirements for practical applications.

Ultimately, the closed-form GMF $\mathbf{p}$ can be designed offline via the transmit sequence $\mathbf{s}$ and the modified oblique projector $\mathbf{E}_{\mathbf{s}|\mathbf{A}}$, which is given by:

$$\mathbf{p}=\mathbf{E}_{\mathbf{s}|\mathbf{A}}^H\mathbf{s}=\mathbf{P}_{\mathbf{A}}^{\perp}\mathbf{s}(\mathbf{s}^H\mathbf{P}_{\mathbf{A}}^{\perp}\mathbf{s})^{-1}\mathbf{s}^H\mathbf{s}. \tag{16}$$

Especially, if $L_A=0$, we have $\mathbf{P}_{\mathbf{A}}^{\perp}=\mathbf{I}_{L\times L}$, and the designed GMF degenerates into the standard MF, i.e., $\mathbf{p}=\mathbf{s}$.

For the scenario of suppressing correlation sidelobes around the mainlobe, $\mathbf{A}$ can be specifically constructed as:

$$\mathbf{A}=[\mathbf{J}_{-L_1}\mathbf{s},\cdots,\mathbf{J}_{-2}\mathbf{s},\mathbf{J}_{-1}\mathbf{s},\mathbf{J}_1\mathbf{s},\mathbf{J}_2\mathbf{s},\cdots,\mathbf{J}_{L_2}\mathbf{s}] \tag{17}$$

where $L_1$ and $L_2$ represent the lag index and $L_1+L_2=L_A$. For the sake of clarity, Fig. 2 depicts a schematic diagram of the construction method of $\mathbf{A}$. If $\mathbf{s}\notin\mathcal{R}(\mathbf{A})$, we can obtain that each transmit sequence corresponds to a specific GMF, indicating that the designed GMF can be compatible with various transmit sequences.

It should be admitted that deriving exact conditions on $\mathbf{s}$ and $\Omega_s^{\|}$ to guarantee $\mathbf{s}\notin\mathcal{R}(\mathbf{A})$ remains a challenge. As an effort to tackle this challenge, Proposition 1 introduces a relatively strict construction strategy for $\Omega_s^{\|}$ that ensures $\mathbf{s}\notin\mathcal{R}(\mathbf{A})$ (i.e., $\mathbf{E}_{\mathbf{s}|\mathbf{A}}$ is effective) independent of the specific form of transmit sequence $\mathbf{s}$.

*Proposition 1:* Define the set $\tilde{\Omega}_s^{\|}$, which includes the following three cases:

Case 1: $\tilde{\Omega}_s^{\|}=\{-L+1,-L+2,\cdots,-1\}$.

Case 2: $\tilde{\Omega}_s^{\|}=\{1,2,\cdots,L-1\}$.

Case 3: Let $2\leq l\leq L-1$, $\tilde{\Omega}_s^{\|}$ takes the form of

$$\begin{aligned}\tilde{\Omega}_s^{\|}=&\{-L+1,-L+2,\cdots,-l\}\\&\cup\{L-l+1,L-l+2,\cdots,L-1\}.\end{aligned}$$

For any of the above cases, if the constructed set of interested lags (i.e., $\Omega_s^{\|}$) satisfies $\Omega_s^{\|}\neq\varnothing$ and $\Omega_s^{\|}\subseteq\tilde{\Omega}_s^{\|}$, then $\mathbf{s}\notin\mathcal{R}(\mathbf{A})$ is guaranteed to hold, independent of the specific form of $\mathbf{s}$.

*Proof:* See Appendix A. ■

From (16), it can be readily observed that the GMF performance varies for different transmit sequences. In the following, we conduct a detailed performance analysis of GMF.

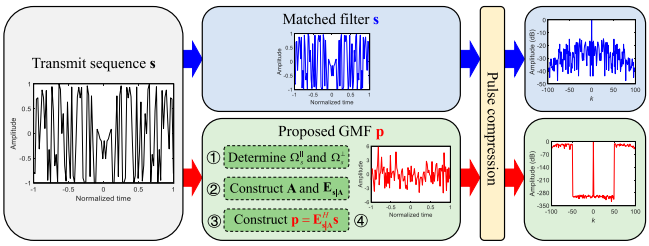


Fig. 3. Comparison diagram of the PC process of standard MF $\mathbf{s}$ and proposed GMF $\mathbf{p}$ for signal $\mathbf{s}$.

### B. Performance Advantages of Proposed GMF

In this part, we assess the performance advantages of the proposed GMF in terms of aperiodic cross-correlation function (ACF) and range resolution.

*1) The ACF Advantage:* Similar to (10), by combining (14) and (16), the ACF $\chi_{\mathbf{s},\mathbf{p}}(k)$ of transmit sequence $\mathbf{s}$ and designed GMF $\mathbf{p}$ is given by:

$$\chi_{\mathbf{s},\mathbf{p}}(k) = \mathbf{p}^H \mathbf{J}_k \mathbf{s} = \mathbf{s}^H \mathbf{E}_{\mathbf{s}|\mathbf{A}} \mathbf{J}_k \mathbf{s} = \begin{cases} \mathbf{s}^H\mathbf{s}, & k=0 \\ \alpha_k(\mathbf{s}) \quad \mathbf{s}^H\mathbf{s}=0, & k \in \Omega_s^{\perp} \\ \alpha_k(\mathbf{s})\mathbf{s}^H\mathbf{s} \neq 0, & k \in \Omega_s^{\parallel} \end{cases} \tag{18}$$

where

$$\alpha_k(\mathbf{s}) = (\mathbf{s}^H \mathbf{P}_{\mathbf{A}}^{\perp} \mathbf{s})^{-1} \mathbf{s}^H \mathbf{P}_{\mathbf{A}}^{\perp} \mathbf{J}_k \mathbf{s}. \tag{19}$$

For the sake of clarity, Fig. 3 presents a brief comparison diagram of the PC process of standard MF and proposed GMF for signal $\mathbf{s}$. From (18) and Fig. 3, leveraging the designed GMF, when $k=0$, the peak correlation level $\chi_{\mathbf{s},\mathbf{p}}(0) = \mathbf{s}^H\mathbf{s}$ remains compared to the peak correlation level $\chi_{\mathbf{s},\mathbf{s}}(0)$ of using MF. For interested lags (i.e., $k \in \Omega_s^{\parallel}$), the correlation level $\chi_{\mathbf{s},\mathbf{p}}(k) = 0$, the GMF can achieve a zero correlation zone, whereas the MF cannot. For uninterested lags (i.e., $k \in \Omega_s^{\perp}$), the correlation level $\chi_{\mathbf{s},\mathbf{p}}(k) = \alpha_k(\mathbf{s})\mathbf{s}^H\mathbf{s}$, related to the transmit sequence. Although the peak correlation level has not deteriorated, the next subsection demonstrates that the GMF shown in (16) enlarges the output noise power, thereby reducing the output SNR compared to the MF. Additionally, the sidelobe levels at uninterested lags (i.e., $\alpha_k(\mathbf{s}), k \in \Omega_s^{\perp}$) vary across different transmit sequences, and can be further suppressed through appropriate sequence design.

*2) The High Range Resolution Advantage:* It is well-known that the AAF mainlobe width by employing the standard MF is $1/B_s$, where $B_s$ denotes the signal bandwidth [2]. This demonstrates that, within the MF framework, the achievable range resolution is limited by the signal bandwidth $B_s$.

For GMF, it is presented as a mismatched filter. Under such cases, traditional range resolution analysis methods based on the MF framework are no longer applicable. Therefore, we analyze the range resolution of GMF through its ACF. To begin with, it should be noted that the proposed GMF is constructed via the discrete transmit sequence. For a continuous transmit waveform $w(t), t \in [0, T]$, where $t$ is the fast time and $T$ denotes the signal time width. With sampling frequency $f_s$, i.e, the sampling time interval

$$\Delta t = \frac{1}{f_s}. \tag{20}$$

The discrete transmit sequence $\mathbf{s}$ in (4) can be re-expressed as $\mathbf{s}_{\Delta t} \in \mathbb{C}^{\lfloor T f_s \rfloor}$, we have:

$$\mathbf{s}_{\Delta t} = \left[w\left(0 \cdot \Delta t\right), w\left(1 \cdot \Delta t\right), \cdots, w\left(\left(\lfloor T f_s \rfloor - 1\right) \cdot \Delta t\right)\right]^T$$

where $\lfloor T f_s \rfloor = L$. Accordingly, the signal with a time shift of $k \cdot \Delta t$ can be denoted as $\mathbf{J}_k \mathbf{s}_{\Delta t}, k = \pm 1, \cdots, \pm(\lfloor T f_s \rfloor - 1)$.

For a high range resolution, the ACF mainlobe is expected to resemble an impulse response. To this end, the GMF $\mathbf{p}_{\Delta t}$ can be designed by $\mathbf{s}_{\Delta t}$ and corresponding $\mathbf{E}_{\mathbf{s}_{\Delta t}|\mathbf{A}_{\Delta t}}$ to suppress sidelobes around the mainlobe. With the mainlobe peak aligned at $t=0$, the interested sidelobe region corresponds to the following set of time lags:

$$t \in \{-k_{1,\max} \cdot \Delta t, \cdots, -1 \cdot \Delta t\} \cup \{1 \cdot \Delta t, \cdots, k_{2,\max} \cdot \Delta t\}$$

where $k_{1,\max} \cdot \Delta t$ ($k_{2,\max} \cdot \Delta t$) is the time interval between the mainlobe and the farthest left (right) sidelobe region of interest. Leveraging the analysis in (18), if $\mathbf{s}_{\Delta t} \notin \mathcal{R}(\mathbf{A}_{\Delta t})$, the ACF within the GMF framework can be further reformulated as a discrete-time delay presentation:

$$\begin{cases} \chi_{\mathbf{s}_{\Delta t},\mathbf{p}_{\Delta t}}(-k_{1,\max}) = \mathbf{p}_{\Delta t}^H \mathbf{J}_{-k_{1,\max}} \mathbf{s}_{\Delta t} = 0 \\ \vdots \\ \chi_{\mathbf{s}_{\Delta t},\mathbf{p}_{\Delta t}}(-1) = \mathbf{p}_{\Delta t}^H \mathbf{J}_{-1} \mathbf{s}_{\Delta t} = 0 \\ \chi_{\mathbf{s}_{\Delta t},\mathbf{p}_{\Delta t}}(0) = \mathbf{p}_{\Delta t}^H \mathbf{s}_{\Delta t} = \mathbf{s}_{\Delta t}^H \mathbf{s}_{\Delta t} \\ \chi_{\mathbf{s}_{\Delta t},\mathbf{p}_{\Delta t}}(1) = \mathbf{p}_{\Delta t}^H \mathbf{J}_{1} \mathbf{s}_{\Delta t} = 0 \\ \vdots \\ \chi_{\mathbf{s}_{\Delta t},\mathbf{p}_{\Delta t}}(k_{2,\max}) = \mathbf{p}_{\Delta t}^H \mathbf{J}_{k_{2,\max}} \mathbf{s}_{\Delta t} = 0. \end{cases} \tag{21}$$

According to (21), it indicates that the GMF framework can achieve an effective impulse response, and the mainlobe width (range resolution) is directly proportional to sampling time interval $\Delta t$ and inversely proportional to sampling frequency $f_s$. As a result, for fixed $B_s$, the GMF can offer a higher range resolution by increasing $f_s$. It should be clarified that increased $f_s$ only increases the number of temporal sampling points, but does not expand the overall lag region of interest, i.e., $k_{1,\max} \cdot \Delta t + k_{2,\max} \cdot \Delta t$.

For the sake of expression, we take the phase coded sequence $\mathbf{s}_{\text{code}} \in \mathbb{C}^L$ as an example. With increased $f_s$, i.e., each symbol in $\mathbf{s}_{\text{code}}$ is consecutively sampled $\varsigma$ times, where $\varsigma \geq 1$ is the user-defined scale factor related to the increased $f_s$. More intuitively, the lag interval (i.e., the sampling time interval) as

shown in Fig. 2 is reduced by $\varsigma$ times. The resulting signal $\breve{\mathbf{s}} \in \mathbb{C}^{\varsigma L}$ can be mathematically formulated as:

$$\breve{\mathbf{s}} = \mathbf{s}_{\text{code}} \otimes \mathbf{1}_{\varsigma}. \tag{22}$$

The matrix $\breve{\mathbf{A}} \in \mathbb{C}^{\varsigma L \times L_{\breve{A}}}$ consists of $L_{\breve{A}}$ time shifted versions of $\breve{\mathbf{s}}$ at the lags $\breve{\Omega}_s^{\|}$ (around the mainlobe), can be denoted as:

$$\breve{\mathbf{A}} = \left[\breve{\mathbf{J}}_{\breve{k}}^{(1)}\breve{\mathbf{s}}, \breve{\mathbf{J}}_{\breve{k}}^{(2)}\breve{\mathbf{s}}, \cdots, \breve{\mathbf{J}}_{\breve{k}}^{(L_{\breve{A}})}\breve{\mathbf{s}}\right], \ \breve{k} \in \breve{\Omega}_s^{\|} \tag{23}$$

where $\breve{\mathbf{J}}_{\breve{k}} \in \mathbb{C}^{\varsigma L \times \varsigma L}$ is the aperiodic shifting matrix similar to $\mathbf{J}_k$ in (9), and $\breve{k}$ is the lag index in increased sampling frequency scenarios. To approximately keep the same lag region of interest under varying sampling frequencies, it is reasonable to set $L_{\breve{A}} = \varsigma L_A$. The GMF for increased sampling frequency scenarios can be constructed by:

$$\breve{\mathbf{p}} = \mathbf{E}_{\breve{\mathbf{s}}|\breve{\mathbf{A}}}^H \breve{\mathbf{s}} = \mathbf{P}_{\breve{\mathbf{A}}}^{\perp}\breve{\mathbf{s}}(\breve{\mathbf{s}}^H \mathbf{P}_{\breve{\mathbf{A}}}^{\perp}\breve{\mathbf{s}})^{-1}\breve{\mathbf{s}}^H\breve{\mathbf{s}}. \tag{24}$$

From (22) and (24), on the one hand, increasing $f_s$ can reduce the lag interval. On the other hand, GMF can suppress the correlation sidelobes around $\breve{k} = 0$ (i.e., the lag at mainlobe). Therefore, the high range resolution can be achieved within the GMF framework by increasing $f_s$. However, it should also be clarified that increasing $f_s$ gives rise to a cost on other aspects of GMF performance, as discussed in Section III-D.

### C. Output SNR Performance of GMF

In addition to zero correlation and high range resolution, the GMF output SNR performance is also a critical factor for precise range profile extraction, especially in scenarios with low input SNR. In this part, we study the output SNR performance of the designed GMF. To begin with, let us briefly demonstrate the output SNR performance of MF $\mathbf{s}$ and general mismatched filter $\mathbf{h}$. For the sake of illustration, we account for the case of a solitary point target (i.e., $\mathbf{Z}(n) = \text{Diag}\{z(n), z(n), \cdots, z(n)\}$) in the presence of white noise. Assuming $\mathbf{n} \in \mathbb{C}^L$ is the noise signal with covariance matrix $\mathbf{R}_{\mathbf{n}} = \mathbb{E}\left\{\mathbf{n}^H\mathbf{n}\right\} = \sigma^2\mathbf{I}_{L\times L}$, where $\sigma^2$ is the noise power. The output SNR gain of implementing $\mathbf{s}$ and $\mathbf{h}$ satisfies the following relationship:

$$\begin{aligned}\widetilde{\text{SNR}}_{\mathbf{h}} &= \frac{|z(n)|^2|\mathbf{h}^H\mathbf{s}|^2}{\mathbf{h}^H\mathbb{E}\left\{\mathbf{n}\mathbf{n}^H\right\}\mathbf{h}} \Big/ \frac{|z(n)|^2}{\sigma^2} = \frac{|\mathbf{h}^H\mathbf{s}|^2}{\mathbf{h}^H\mathbf{h}} \\ &\le \widetilde{\text{SNR}}_{\mathbf{s}} = \frac{|\mathbf{s}^H\mathbf{s}|^2}{\mathbf{s}^H\mathbf{s}} = \mathbf{s}^H\mathbf{s}.\end{aligned} \tag{25}$$

Leveraging the Cauchy-Schwarz inequality, $\widetilde{\text{SNR}}_{\mathbf{h}} = \widetilde{\text{SNR}}_{\mathbf{s}}$ if and only if $\mathbf{h} \propto \mathbf{s}$. To suppress correlation sidelobe levels while ensuring the output SNR performance, existing methods attempt to constrain $\|\mathbf{h} - \mathbf{s}\|_2^2$ ($|\mathbf{h}^H\mathbf{s}|^2$) to be less (greater) than a preset threshold [40], [41]. However, there is currently no theoretical basis for determining the optimal threshold, thus these approaches may not solve the above trade-off effectively.

Similarly, the output SNR gain of implementing the GMF $\mathbf{p}$ satisfies the following relationship:

$$\widetilde{\text{SNR}}_{\mathbf{p}} = \frac{|z(n)|^2|\mathbf{s}^H\mathbf{E}_{\mathbf{s}|\mathbf{A}}\mathbf{s}|^2}{\mathbf{s}^H\mathbf{E}_{\mathbf{s}|\mathbf{A}}\mathbb{E}\{\mathbf{n}\mathbf{n}^H\}\mathbf{E}_{\mathbf{s}|\mathbf{A}}^H\mathbf{s}} \Big/ \frac{|z(n)|^2}{\sigma^2} \tag{26a}$$

$$= \frac{|\mathbf{s}^H\mathbf{s}|^2}{\mathbf{s}^H\mathbf{E}_{\mathbf{s}|\mathbf{A}}\mathbf{E}_{\mathbf{s}|\mathbf{A}}^H\mathbf{s}} \tag{26b}$$

$$= \mathbf{s}^H\mathbf{s} - \mathbf{s}^H\mathbf{P}_{\mathbf{A}}\mathbf{s} \tag{26c}$$

$$= \widetilde{\text{SNR}}_{\mathbf{s}} - \mathbf{s}^H\mathbf{P}_{\mathbf{A}}\mathbf{s} \tag{26d}$$

where we have utilized the fact that $\mathbf{P}_{\mathbf{A}}^{\perp}\mathbf{P}_{\mathbf{A}}^{\perp} = \mathbf{P}_{\mathbf{A}}^{\perp}$. For any transmit sequence $\mathbf{s} \neq \mathbf{0}_L$, since orthogonal projector $\mathbf{P}_{\mathbf{A}} \succeq \mathbf{0}_{L\times L}$, we have $\mathbf{s}^H\mathbf{P}_{\mathbf{A}}\mathbf{s} \ge 0$. In addition, from (13), one can easily derive that $\mathbf{s}^H\mathbf{s} > \mathbf{s}^H\mathbf{P}_{\mathbf{A}}\mathbf{s}$. Based on these foundations, we have

$$0 < \widetilde{\text{SNR}}_{\mathbf{p}} \le \widetilde{\text{SNR}}_{\mathbf{s}}. \tag{27}$$

$\widetilde{\text{SNR}}_{\mathbf{p}} = \widetilde{\text{SNR}}_{\mathbf{s}}$ if and only if $\mathbf{s} \in \mathcal{R}^{\perp}(\mathbf{A})$.

From (18) and (26), although the peak ACF level is preserved by using GMF $\mathbf{p}$, it enlarges the output noise power, resulting in output SNR loss. With the white noise assumption, the output SNR loss is $\mathbf{s}^H\mathbf{P}_{\mathbf{A}}\mathbf{s}$, which is related to the transmit sequence $\mathbf{s}$. Apparently, by designing $\mathbf{s}$ to minimize $\mathbf{s}^H\mathbf{P}_{\mathbf{A}}\mathbf{s}$, the output SNR loss can be reduced. However, the above metric relies heavily on the white noise assumption. Under colored noise conditions, this metric may no longer be applicable. Meantime, from (18), this metric cannot be directly employed to suppress sidelobes at uninterested lags, i.e., $\alpha_k(\mathbf{s}), k \in \Omega_s^{\perp}$.

### D. Robust Design Metric and Further Analysis

To overcome the aforementioned challenges, a robust design metric is introduced and used to analyze the cost of achieving high range resolution within the GMF framework.

*1) Robust Design Metric:* To begin with, we investigate a robust metric for designing the enhanced GMF. This metric is expected to be applicable to a broader range of scenarios, including colored noise backgrounds and sidelobe suppression at uninterested lags, rather than being limited to the case of white noise. If the exact covariance $\mathbf{R}_c$ of the colored disturbance is available, the output SNR loss can be modified by substituting $\mathbb{E}\{\mathbf{n}\mathbf{n}^H\} = \mathbf{R}_c$ into (26a), from which the design metric is obtained. In practical radar environments, it is challenging to accurately obtain both the statistical characteristics of colored noise and $\mathbf{J}_k\mathbf{s}, k \in \Omega_s^{\perp}$. To this end, we investigate the filtering results of the GMF $\mathbf{p}$ for any signal $\mathbf{a} \neq \mathbf{0}_L \in \mathbb{C}^L$, see Proposition 2 for details.

*Proposition 2:* For any vector $\mathbf{a} \in \mathbb{C}^L$ and $\|\mathbf{a}\|_2 \neq 0$, the projection of oblique projector $\mathbf{E}_{\mathbf{s}|\mathbf{A}}$ on vector $\mathbf{a}$ is

$$\mathbf{E}_{\mathbf{s}|\mathbf{A}}\mathbf{a} = \beta\mathbf{s}, \ 0 \le |\beta| \le \|\mathbf{a}\|_2(\mathbf{s}^H\mathbf{s} - \mathbf{s}^H\mathbf{P}_{\mathbf{A}}\mathbf{s})^{-\frac{1}{2}}. \tag{28}$$

The filtering output amplitude of $\mathbf{p}$ for signal $\mathbf{a}$ obeys

$$\begin{aligned}0 \le \left|\mathbf{p}^H\mathbf{a}\right| &= \left|\mathbf{s}^H\mathbf{E}_{\mathbf{s}|\mathbf{A}}\mathbf{a}\right| = |\beta|\,\mathbf{s}^H\mathbf{s} \\ &\le \|\mathbf{a}\|_2 \underbrace{\mathbf{s}^H\mathbf{s}(\mathbf{s}^H\mathbf{s} - \mathbf{s}^H\mathbf{P}_{\mathbf{A}}\mathbf{s})^{-\frac{1}{2}}}_{=\|\mathbf{p}\|_2}.\end{aligned} \tag{29}$$

*Proof:* See Appendix B. ∎

According to (18) and Proposition 2, we can briefly draw the following conclusions:

- The oblique projector $\mathbf{E}_{\mathbf{s}|\mathbf{A}}$ projects any signal $\mathbf{a}$ onto vector $\mathbf{s}$, with component $|\beta|$ meeting (28).
- No matter how large $\|\mathbf{a}\|_2$ is, the GMF output $\left|\mathbf{p}^H\mathbf{a}\right| = 0$ only for signals at interested lags, i.e., $\mathbf{a} \in \mathcal{R}(\mathbf{A})$.
- For the desired signal, i.e., $\mathbf{a} = z(n)\mathbf{s}$, the GMF output is $|\mathbf{p}^H\mathbf{a}| = |z(n)|\mathbf{s}^H\mathbf{s}$. For undesired signals, such as the noise signal $\mathbf{a} = \mathbf{n}$ and signals at uninterested lags $\mathbf{a} \propto \mathbf{J}_k\mathbf{s}, k \in \Omega_s^{\perp}$, the GMF output satisfies (29) and the maximum output amplitude depends on both the signal amplitude $\|\mathbf{a}\|_2$ and GMF energy (controlled by the transmit sequence $\mathbf{s}$).

Although we cannot access the ideal statistical characteristics of the input undesired signals and control their amplitude $\|\mathbf{a}\|_2$, we can suppress the signals as much as possible by minimizing the GMF energy $\|\mathbf{p}\|_2^2$. From Fig. 3, it is evident that the designed GMF yields a higher energy than the MF. The straightforward approach is to normalize the designed GMF by conducting $\mathbf{p}/\|\mathbf{p}\|_2$. However, this correspondingly results in a loss of peak level, as expressed in (18).

Building on the aforementioned analysis, we propose to design transmit sequence $\mathbf{s}$ to minimize the GMF magnitude (energy) $\|\mathbf{p}\|_2 = \mathbf{s}^H\mathbf{s}(\mathbf{s}^H\mathbf{s} - \mathbf{s}^H\mathbf{P}_{\mathbf{A}}\mathbf{s})^{-\frac{1}{2}}$ ($\|\mathbf{p}\|_2^2$) in (29), thereby introducing a novel sequence design metric. Generally, the transmit sequence to be designed has a limited energy budget, i.e., $\|\mathbf{s}\|_2^2 = e_c^2$ (constant). On this basis, the metric $\mathbf{s}^H\mathbf{s}(\mathbf{s}^H\mathbf{s} - \mathbf{s}^H\mathbf{P}_{\mathbf{A}}\mathbf{s})^{-\frac{1}{2}}$ evolves to

$$e_c^2(e_c^2 - \mathbf{s}^H\mathbf{P}_{\mathbf{A}}\mathbf{s})^{-\frac{1}{2}}. \tag{30}$$

According to (30), we can see that the GMF energy decreases as $\mathbf{s}^H\mathbf{P}_{\mathbf{A}}\mathbf{s}$ decreases. Especially, if $\mathbf{s}^H\mathbf{P}_{\mathbf{A}}\mathbf{s} = 0$, i.e., $\mathbf{s} \in \mathcal{R}^{\perp}(\mathbf{A})$, the GMF achieves a minimum energy, which equals that of MF. For the sake of illustration, we define the relative GMF energy as the ratio of GMF energy and MF energy, i.e.,

$$\frac{\|\mathbf{p}\|_2^2}{\|\mathbf{s}\|_2^2} = \frac{\mathbf{s}^H\mathbf{s}}{\mathbf{s}^H\mathbf{s} - \mathbf{s}^H\mathbf{P}_{\mathbf{A}}\mathbf{s}} = \frac{1}{1 - \frac{\mathbf{s}^H\mathbf{P}_{\mathbf{A}}\mathbf{s}}{\mathbf{s}^H\mathbf{s}}} = \frac{1}{1 - \frac{\mathbf{s}^H\mathbf{P}_{\mathbf{A}}\mathbf{s}}{e_c^2}}. \tag{31}$$

It is evident that the relative GMF energy decreases as $\mathbf{s}^H\mathbf{P}_{\mathbf{A}}\mathbf{s}$ decreases, with a minimum value of 1. By designing $\mathbf{s}$, we can optimize the metric $\mathbf{s}^H\mathbf{P}_{\mathbf{A}}\mathbf{s}$ to minimize the GMF energy or relative GMF energy, thus suppressing undesired signals, including but not limited to noise $\mathbf{n}$ and $\mathbf{J}_k\mathbf{s}, k \in \Omega_s^{\perp}$.

Interestingly, the derived metric $\mathbf{s}^H\mathbf{P}_{\mathbf{A}}\mathbf{s}$ is identical to the output SNR loss in (26) under the white noise. Although the metric are derived from different perspectives, they ultimately lead to the same formulation. However, it is worth noting that the resulting metric is relatively relaxed. While it may not be the optimal choice in a strict theoretical sense, it offers improved robustness in practical radar environments. In this way, this metric can be applied even if the white noise assumption does not hold. Meanwhile, the correlation sidelobes at uninterested lags, i.e., $\alpha_k(\mathbf{s}), k \in \Omega_s^{\perp}$, can also be controlled by employing this metric. It is also important to note that for the same transmit sequence $\mathbf{s}$, the larger $L_A$ is, the smaller the dimension of subspace $\mathcal{R}^{\perp}(\mathbf{A})$ is, and $\mathbf{s}^H\mathbf{P}_{\mathbf{A}}\mathbf{s}$ increases. That is to say, for the same $\mathbf{s}$, the larger lag region of interest, the larger output level of GMF for undesired signals.

*2) Cost of Achieving High Range Resolution:* As analyzed in Section III-B, increasing $f_s$ can improve the range resolution of GMF $\mathbf{p}_{\Delta t}$. However, the effect of increasing $f_s$ on the GMF energy has not been investigated. As previously discussed, a higher GMF energy amplifies the output power of undesired signals, degrading the output SNR and elevating the sidelobe level at uninterested lags. In view of the fact that $\mathbf{s}_{\Delta t}^H\mathbf{s}_{\Delta t}$ increases with $f_s$, we next analyze the variation trend of the relative GMF energy in (31), i.e.,

$$\frac{\|\mathbf{p}_{\Delta t}\|_2^2}{\|\mathbf{s}_{\Delta t}\|_2^2} = \frac{1}{1 - \frac{\mathbf{s}_{\Delta t}^H\mathbf{P}_{\mathbf{A}_{\Delta t}}\mathbf{s}_{\Delta t}}{\mathbf{s}_{\Delta t}^H\mathbf{s}_{\Delta t}}} \tag{32}$$

with respect to (w.r.t.) $f_s$. The lag region of interest is fixed. As we can see from (32), this is equivalent to analyzing how $\mathbf{s}_{\Delta t}^H\mathbf{P}_{\mathbf{A}_{\Delta t}}\mathbf{s}_{\Delta t}/\mathbf{s}_{\Delta t}^H\mathbf{s}_{\Delta t}$ varies w.r.t. $f_s$. To begin with, it is evident that

$$\mathbf{J}_1\mathbf{s}_{\Delta t} \in \mathcal{R}(\mathbf{A}_{\Delta t}),\ \frac{\mathbf{s}_{\Delta t}^H\mathbf{J}_1\mathbf{s}_{\Delta t}}{\mathbf{s}_{\Delta t}^H\mathbf{s}_{\Delta t}} = \frac{\chi_{\mathbf{s}_{\Delta t},\mathbf{s}_{\Delta t}}(1)}{\chi_{\mathbf{s}_{\Delta t},\mathbf{s}_{\Delta t}}(0)}. \tag{33}$$

With the Cauchy-Schwarz inequality, we have

$$|\mathbf{s}_{\Delta t}^H\mathbf{J}_1\mathbf{s}_{\Delta t}| = |\mathbf{s}_{\Delta t}^H\mathbf{P}_{\mathbf{A}_{\Delta t}}\mathbf{J}_1\mathbf{s}_{\Delta t}| \le |\mathbf{P}_{\mathbf{A}_{\Delta t}}\mathbf{s}_{\Delta t}|_2 \cdot |\mathbf{J}_1\mathbf{s}_{\Delta t}|_2.$$

Using the facts that $|\mathbf{J}_1\mathbf{s}_{\Delta t}|_2^2 < |\mathbf{s}_{\Delta t}|_2^2$ and $\mathbf{s}_{\Delta t} \notin \mathcal{R}(\mathbf{A}_{\Delta t})$, we then have

$$\left|\frac{\chi_{\mathbf{s}_{\Delta t},\mathbf{s}_{\Delta t}}(1)}{\chi_{\mathbf{s}_{\Delta t},\mathbf{s}_{\Delta t}}(0)}\right|^2 < \frac{\mathbf{s}_{\Delta t}^H\mathbf{P}_{\mathbf{A}_{\Delta t}}\mathbf{s}_{\Delta t}}{\mathbf{s}_{\Delta t}^H\mathbf{s}_{\Delta t}} < 1. \tag{34}$$

For the MF $\mathbf{s}_{\Delta t}$, it is well-known that the mainlobe width of AAF $\chi_{\mathbf{s}_{\Delta t},\mathbf{s}_{\Delta t}}$ is inversely related to $B_s$, independent of $f_s$. Generally, for practical applications, the sampling frequency meets $f_s \ge B_s$, i.e, $\Delta t \le 1/B_s$. For fixed $B_s$, leveraging the monotonicity within the mainlobe region of AAF $\chi_{\mathbf{s}_{\Delta t},\mathbf{s}_{\Delta t}}$, as $f_s$ increases, the lag interval $\Delta t$ decreases, while $|\chi_{\mathbf{s}_{\Delta t},\mathbf{s}_{\Delta t}}(1)|$ increases and approaches $|\chi_{\mathbf{s}_{\Delta t},\mathbf{s}_{\Delta t}}(0)|$. Thereby, it is not difficult to find that $|\chi_{\mathbf{s}_{\Delta t},\mathbf{s}_{\Delta t}}(1)/\chi_{\mathbf{s}_{\Delta t},\mathbf{s}_{\Delta t}}(0)|$ increases with $f_s$. On this basis, the feasible range of $\mathbf{s}_{\Delta t}^H\mathbf{P}_{\mathbf{A}_{\Delta t}}\mathbf{s}_{\Delta t}/\mathbf{s}_{\Delta t}^H\mathbf{s}_{\Delta t}$ progressively shrinks as $f_s$ increases. Specifically, when $f_s \to +\infty$, we can obtain the following limit:

$$\lim_{f_s \to +\infty}\left|\frac{\chi_{\mathbf{s}_{\Delta t},\mathbf{s}_{\Delta t}}(1)}{\chi_{\mathbf{s}_{\Delta t},\mathbf{s}_{\Delta t}}(0)}\right| \to 1,\ \lim_{f_s \to +\infty}\frac{\mathbf{s}_{\Delta t}^H\mathbf{P}_{\mathbf{A}_{\Delta t}}\mathbf{s}_{\Delta t}}{\mathbf{s}_{\Delta t}^H\mathbf{s}_{\Delta t}} \to 1. \tag{35}$$

According to (34) and (35), it is reasonable to infer that the overall trend of $\mathbf{s}_{\Delta t}^H\mathbf{P}_{\mathbf{A}_{\Delta t}}\mathbf{s}_{\Delta t}/\mathbf{s}_{\Delta t}^H\mathbf{s}_{\Delta t}$ increases with $f_s$. However, this does not imply that $\mathbf{s}_{\Delta t}^H\mathbf{P}_{\mathbf{A}_{\Delta t}}\mathbf{s}_{\Delta t}/\mathbf{s}_{\Delta t}^H\mathbf{s}_{\Delta t}$ increases strictly monotonically with $f_s$. Despite $B_s$ and the lag region of interest being fixed, the specific elements vary with different sequences. Based on the aforementioned analysis, it is reasonable to conclude that the relative GMF energy exhibits an increasing trend w.r.t. $f_s$.

In short, compared to the MF, the range resolution within the GMF framework can be improved by increasing the sampling frequency $f_s$. However, the relative GMF energy exhibits an increasing trend with $f_s$, which will lead to a larger output energy of undesired signals, particularly when $f_s \to +\infty$. Thereby, the output SNR and the sidelobe levels at uninterested lags show a deteriorating trend as $f_s$ increases. As a consequence,

within the GMF framework, it should be clarified that $f_s$ cannot be increased arbitrarily in pursuit of extremely high range resolution.

Based on the above discussion, the GMF performance is closely related to the lag region of interest, $B_s$, and $f_s$. For practical applications, to enable weak target detection and achieve a high-resolution range profile without increasing the hardware complexity. We introduce a feasible construct strategy for GMF from three perspectives. First, select a general (rather than ultra-wideband) $B_s$ to alleviate the hardware burden. Second, construct the interested lag set around the mainlobe and determine the minimum $L_A$ according to the range distribution region of the targets. Finally, adjust $f_s$ via the relative GMF energy shown in (31) to balance an acceptable output SNR loss and desired range resolution.

### E. Design for Enhanced GMF

In light of the derived robust metric, this subsection puts forward the design strategy for enhanced GMF. Besides $\|\mathbf{s}\|_2^2 = e_c^2$, with additional constraints of interest, such as constant modulus, peak-to-average ratio, discrete phase constraints, etc [22]. Let set $\mathcal{S}$ denote these interested constraints, the sequence design for the enhanced GMF can be formulated as

$$\min_{\mathbf{s}\in\mathcal{S}} \ \mathbf{s}^H\mathbf{P}_{\mathbf{A}}\mathbf{s}. \tag{36}$$

Herein, for the sake of illustration and example, we impose a constant modulus constraint on $\mathbf{s}$ to maximize transmitter efficiency. Problem (36) can thus be recast as follows:

$$\min_{\mathbf{s}} \ \mathbf{s}^H\mathbf{P}_{\mathbf{A}}\mathbf{s} \quad \text{s.t.} \ \ |s(l)|^2 = 1, l = 1, 2, \cdots, L. \tag{37}$$

Since $\mathbf{P}_{\mathbf{A}}$ is a function of $\mathbf{s}$, (37) is a sixth-order optimization problem w.r.t. $\mathbf{s}$ under $L$ quadratic equality constraints. It should be noted that developing advanced solution algorithms for problem (37) is not the focus of this paper, as the primary contribution lies in the proposed GMF design framework. To solve this non-convex problem, we use the coordinate descent (CD) iterative framework [23] to sequentially minimize our objective over one variable keeping fixed the others, resulting in a suboptimal $\mathbf{s}^\star$. Specifically, we first initialize a random phase sequence $\mathbf{s}^{(0)}$, for $(i_t)$th iteration (referred to as the outer loop), $l$th code entry $s_l^{(i_t-1)}$ is selected as the optimization variable leading to the following problem at step $(l)$ (referred to as the inner loop):

$$\begin{aligned} s_l^{(i_t)} &= \arg\min_{s_l^{(i_t-1)}} \ \left(\mathbf{s}_l^{(i_t)}\right)^H \mathbf{P}_{\mathbf{A}_l^{(i_t)}} \mathbf{s}_l^{(i_t)} \\ \text{s.t.} \ \ s_l^{(i_t-1)} &= e^{j\phi}, \ \phi \in \frac{2\pi}{M}\{0, 1, \cdots, M-1\} \end{aligned} \tag{38}$$

where $M$ is the number of discrete phases, and

$$\mathbf{s}_l^{(i_t)} = [s_1^{(i_t)}, \cdots, s_{l-1}^{(i_t)}, s_l^{(i_t-1)}, s_{l+1}^{(i_t-1)}, \cdots, s_L^{(i_t-1)}]. \tag{39}$$

$\mathbf{P}_{\mathbf{A}_l^{(i_t)}}$ is constructed with $\mathbf{s}_l^{(i_t)}$ as described in Section III-A. After obtaining $s_l^{(i_t)}$, the $(l+1)$th inner loop begins. Once the inner loop concludes, the $(i_t+1)$th outer loop starts. Repeating the above process until the following condition is satisfied:

$$\left(\mathbf{s}^{(i_t+1)}\right)^H \mathbf{P}_{\mathbf{A}^{(i_t+1)}} \mathbf{s}^{(i_t+1)} - \left(\mathbf{s}^{(i_t)}\right)^H \mathbf{P}_{\mathbf{A}^{(i_t)}} \mathbf{s}^{(i_t)} \le \xi \tag{40}$$

where $\xi$ represents the preset convergence threshold. It can be readily verified that the objective function is bounded since $0 \le \mathbf{s}^H\mathbf{P}_{\mathbf{A}}\mathbf{s} \le \mathbf{s}^H\mathbf{s}$. Thereby, the monotonicity of the CD iterative framework and the boundedness of the objective function are sufficient to guarantee the convergence of the objective value [23]. From (13), $\mathbf{s} \notin \mathcal{R}(\mathbf{A})$ holds if and only if $\mathbf{s}^H\mathbf{P}_{\mathbf{A}}\mathbf{s} < \|\mathbf{s}\|_2^2$. Owing to the constant transmit sequence energy and monotonically decreasing objective function value, if $\mathbf{s}^{(0)} \notin \mathcal{R}(\mathbf{A}^{(0)})$, i.e., $(\mathbf{s}^{(0)})^H\mathbf{P}_{\mathbf{A}^{(0)}}\mathbf{s}^{(0)} < \|\mathbf{s}^{(0)}\|_2^2$ holds, we can find that:

$$\begin{aligned} \left(\mathbf{s}^{(i_t+1)}\right)^H \mathbf{P}_{\mathbf{A}^{(i_t+1)}} \mathbf{s}^{(i_t+1)} &\le \left(\mathbf{s}^{(i_t)}\right)^H \mathbf{P}_{\mathbf{A}^{(i_t)}} \mathbf{s}^{(i_t)} \\ &\le \cdots \le (\mathbf{s}^{(0)})^H \mathbf{P}_{\mathbf{A}^{(0)}} \mathbf{s}^{(0)} \\ &< \|\mathbf{s}^{(0)}\|_2^2 = \cdots = \|\mathbf{s}^{(i_t+1)}\|_2^2 = e_c^2. \end{aligned}$$

Thus, as long as $\mathbf{s}^{(0)} \notin \mathcal{R}(\mathbf{A}^{(0)})$, $\mathbf{s}^{(i_t)} \notin \mathcal{R}(\mathbf{A}^{(i_t)})$ is naturally satisfied as the iterations progress.

On this basis, we can achieve a suboptimal sequence $\mathbf{s}^\star$, and the enhanced GMF $\mathbf{p}^\star$ can be constructed with $\mathbf{s}^\star$ and the corresponding oblique projector $\mathbf{E}_{\mathbf{s}^\star|\mathbf{A}^\star}$ via (16), i.e.,

$$\mathbf{p}^\star = \mathbf{E}_{\mathbf{s}^\star|\mathbf{A}^\star}^H \mathbf{s}^\star = \mathbf{P}_{\mathbf{A}^\star}^\perp \mathbf{s}^\star \left((\mathbf{s}^\star)^H \mathbf{P}_{\mathbf{A}^\star}^\perp \mathbf{s}^\star\right)^{-1} (\mathbf{s}^\star)^H \mathbf{s}^\star. \tag{41}$$

Ultimately, the enhanced GMF can be well-designed offline, and then be employed online to conduct PC as efficiently as the MF. The enhanced GMF can achieve zero correlation at interested lags, reduced sidelobe level at uninterested lags, and negligible output SNR loss. The primary distinction between GMF and enhanced GMF is that the latter requires selecting a suboptimal transmit sequence by the formulated optimization.

It is shown that the design process of the enhanced GMF involves the transmit sequence optimization. For the sake of clarity, in this part, we briefly discuss the relationship between the enhanced GMF and existing sequence design methods, including transmit design methods [25], [26], [27], [28], [29] and transceiver design methods [37], [38], [39], [40], [41], [42], summarized in Table I, where set $\mathcal{F}$ represents the constraint set of the receive filter. According to Table I, we can see that when $\mathbf{P}_{\mathbf{A}} \to \mathbf{A}\mathbf{A}^H$ and $\mathbf{p} \to \mathbf{s}$, the proposed method evolves to transmit design methods. When $\mathbf{s}^H\mathbf{P}_{\mathbf{A}}\mathbf{s} \to \mathbf{h}^H\mathbf{A}\mathbf{A}^H\mathbf{h}$ and $\mathbf{p} \to \mathbf{h}$, the proposed method evolves to transceiver design methods. For the proposed GMF, we can theoretically achieve a ZCZ. With the white noise assumption, we have output SNR loss $\xrightarrow{\mathbf{s}}$ 0. However, the maximum lag region of interest is limited.

### F. Computational Complexity

In this subsection, we analyze the complexity of the proposed method. For GMF, the primary calculation lies in the construction of oblique projector $\mathbf{E}_{\mathbf{s}|\mathbf{A}}$, its design complexity is $\mathcal{O}(L_A^3)$. For enhanced GMF, the main calculations include the construction of oblique projector $\mathbf{E}_{\mathbf{s}|\mathbf{A}}$ and the enhanced design of GMF. In this paper, we introduce a CD iterative framework for enhanced GMF, its design complexity is $\mathcal{O}(N_t L M L_A^3)$,

TABLE I
A BRIEF COMPARISON OF ENHANCED GMF WITH EXISTING SEQUENCE DESIGN METHODS

| Method | Optimization variable | Design metric | Advantage | Disadvantage |
|---|---|---|---|---|
| Transmit design | Sequence $\mathbf{s}$ | Sequence: $\min_{\mathbf{s}\in\mathcal{S}} \mathbf{s}^H\mathbf{A}\mathbf{A}^H\mathbf{s}$<br>Filter: matched filter $\mathbf{s}$ | No output SNR loss | Unsatisfied ZCZ performance |
| Transceiver design | Sequence $\mathbf{s}$ and mismatched filter $\mathbf{h}$ | Sequence and filter: $\min_{\mathbf{s}\in\mathcal{S},\mathbf{h}\in\mathcal{F}} \mathbf{h}^H\mathbf{A}\mathbf{A}^H\mathbf{h}$ | Improved ZCZ performance | Output SNR loss |
| Enhanced GMF | Sequence $\mathbf{s}$ | Sequence: $\min_{\mathbf{s}\in\mathcal{S}} \mathbf{s}^H\mathbf{P}_{\mathbf{A}}\mathbf{s}$<br>Filter: $\mathbf{p}^\star = \mathbf{E}^H_{\mathbf{s}^\star\|\mathbf{A}^\star}\mathbf{s}^\star$ | • Zero-correlation within ZCZ<br>• Output SNR loss $\xrightarrow{\mathbf{s}}$ 0 | Maximum number of interested lags is limited |

where $N_t$ is the iteration number of the outer loop, which is of a higher order than the computation of the oblique projector. As a result, the overall design complexity of the enhanced GMF is $\mathcal{O}(N_tLML_A^3)$. For the online pulse compression process, GMF and enhanced GMF, similar to MF, can be implemented in the frequency domain using the fast Fourier transform (FFT), each with a computational complexity of $\mathcal{O}(L\log_2 L)$ per range cell.

## IV. EXTENSIONS OF PROPOSED GMF

Drawing on the above discussion, the proposed GMF is designed for a single transmit sequence without considering the intrapulse Doppler shift. However, it can be readily extended to broader scenarios and applications. Specifically, we focus on two key extensions of the proposed GMF: the first involves scenarios with the intrapulse Doppler shift, and the second addresses cases with multiple transmit sequences.

### A. Scenarios With Intrapulse Doppler Shift

For detecting the high-speed target, intrapulse Doppler shift becomes unavoidable. In this case, denote $\mathbf{d}(f)\in\mathbb{C}^L$ the normalized Doppler shift vector, given by:

$$\mathbf{d}(f)=\left[e^{j2\pi\frac{f}{L}\cdot 1}, e^{j2\pi\frac{f}{L}\cdot 2},\cdots,e^{j2\pi\frac{f}{L}\cdot L}\right]^T \tag{42}$$

where $f\in\left[-\frac{L}{2},\frac{L}{2}\right)$. It is reasonable to assume the target is located within a certain local region $f\in[-f_{\text{loc}},f_{\text{loc}}]$, $f_{\text{loc}}\le\frac{L}{2}$ [38], [41]. Similar to the analysis in Section III-A, the oblique projector can be constructed as follows:

$$\mathbf{E}_{\widetilde{\mathbf{S}}_D|\widetilde{\mathbf{A}}_D}=\widetilde{\mathbf{S}}_D(\widetilde{\mathbf{S}}_D^H\mathbf{P}^{\perp}_{\widetilde{\mathbf{A}}_D}\widetilde{\mathbf{S}}_D)^{-1}\widetilde{\mathbf{S}}_D^H\mathbf{P}^{\perp}_{\widetilde{\mathbf{A}}_D} \tag{43}$$

with

$$\tilde{\mathbf{s}}_k(f)=\mathbf{J}_k\text{Diag}\left\{\mathbf{d}(f)\right\}\mathbf{s},\ k\in\{0,\Omega_s^{\|}\} \tag{44a}$$

$$\widetilde{\mathbf{S}}_k=[\tilde{\mathbf{s}}_k(-f_{\text{loc}}),\cdots,\tilde{\mathbf{s}}_k(f),\cdots,\tilde{\mathbf{s}}_k(f_{\text{loc}})]\in\mathbb{C}^{L\times f_{\text{num}}} \tag{44b}$$

$$\widetilde{\mathbf{S}}_D=\widetilde{\mathbf{S}}_0 \tag{44c}$$

$$\widetilde{\mathbf{A}}_D=\left[\widetilde{\mathbf{S}}_k^{(1)},\widetilde{\mathbf{S}}_k^{(2)},\cdots,\widetilde{\mathbf{S}}_k^{(L_A)}\right]\in\mathbb{C}^{L\times L_A f_{\text{num}}},\ k\in\Omega_s^{\|} \tag{44d}$$

where $f_{\text{num}}$ represents the number of discrete Doppler shift within $[-f_{\text{loc}},f_{\text{loc}}]$. To ensure the effectiveness of constructed oblique projector $\mathbf{E}_{\widetilde{\mathbf{S}}_D|\widetilde{\mathbf{A}}_D}$, the following two points should be noted:

- The value of $f_{\text{num}}$ could be set relatively large to mitigate the off-grid problem between the discrete Doppler shift and actual target Doppler shift.
- Replacing $\widetilde{\mathbf{S}}_k, k\in\{0,\Omega_s^{\|}\}$ by matrix $\mathbf{V}_k, k\in\{0,\Omega_s^{\|}\}$, which is composed of $Q_k, Q_k\ll L$ principal left singular vectors of $\widetilde{\mathbf{S}}_k$. For fixed $\Omega_s^{\|}$ and $\mathbf{s}$, $Q_k$ increases with $f_{\text{loc}}$ and reaches a maximum value of $L$.

On this basis, the oblique projector $\mathbf{E}_{\widetilde{\mathbf{S}}_D|\widetilde{\mathbf{A}}_D}$ can be modified to $\mathbf{E}_{\mathbf{V}_0|\mathbf{A}_D}$ with $\mathbf{A}_D=[\mathbf{V}_k^{(1)},\mathbf{V}_k^{(2)},\cdots,\mathbf{V}_k^{(L_A)}], k\in\Omega_s^{\|}$. To ensure the effectiveness of $\mathbf{E}_{\mathbf{V}_0|\mathbf{A}_D}$, i.e., matrix $[\mathbf{V}_0,\mathbf{A}_D]$ has a full column rank, compared to the scenario without considering intrapulse Doppler shift, the maximum number of interested lags, i.e., $L_A$, must be reduced. Ultimately, the GMF for the scenario with intrapulse Doppler shift can be designed as follows:

$$\mathbf{p}_{\text{Doppler}}=\mathbf{E}^H_{\mathbf{V}_0|\mathbf{A}_D}\mathbf{s}. \tag{45}$$

It should be noted that due to the presence of intrapulse Doppler shift, the peak level yields a slight loss by employing $\mathbf{p}_{\text{Doppler}}$. Therefore, in addition to the enhanced GMF design method demonstrated in Section III-E, the constraint on the Doppler tolerance (peak correlation level) of transmit sequence needs to be incorporated in $\mathcal{S}$.

### B. Scenarios With Multiple Transmit Sequences

For applications such as multi-input multi-output radar, it is typically necessary to transmit multiple sequences. In this case, denote the matrix composed of $U$ linearly independent transmit sequences by $\mathbf{S}=[\mathbf{s}_1,\mathbf{s}_2,\cdots,\mathbf{s}_U]\in\mathbb{C}^{L\times U}$, let $\mathbf{S}_{u-}\in\mathbb{C}^{L\times(U-1)}$ represent the matrix with $\mathbf{s}_u, u=1,2,\cdots,U$ removed from $\mathbf{S}$, and let $\mathbf{S}_{\mathbf{J},u}\in\mathbb{C}^{L\times L_A}$ represent the matrix composed of $L_A$ time shifted versions of $\mathbf{s}_u$ at the interested lags, similar to $\mathbf{A}$, i.e.,

$$\mathbf{S}_{\mathbf{J},u}=\left[\mathbf{J}_k^{(1)}\mathbf{s}_u,\mathbf{J}_k^{(2)}\mathbf{s}_u,\cdots,\mathbf{J}_k^{(L_A)}\mathbf{s}_u\right],\ k\in\Omega_s^{\|}. \tag{46}$$

Then the $u$th GMF for multiple transmit sequence applications can be designed as follows:

$$\mathbf{p}_u=\mathbf{E}^H_{\mathbf{s}_u|\mathbf{A}_u}\mathbf{s}_u=\mathbf{P}^{\perp}_{\mathbf{A}_u}\mathbf{s}_u(\mathbf{s}_u^H\mathbf{P}^{\perp}_{\mathbf{A}_u}\mathbf{s}_u)^{-1}\mathbf{s}_u^H\mathbf{s}_u \tag{47a}$$

$$\mathbf{A}_u=[\mathbf{S}_{u-},\mathbf{S}_{\mathbf{J},1},\mathbf{S}_{\mathbf{J},2},\cdots,\mathbf{S}_{\mathbf{J},U}]\in\mathbb{C}^{L\times(U-1+L_AU)}. \tag{47b}$$

As we can see, for multiple transmit sequence applications, to guarantee that $\mathcal{R}(\mathbf{s}_u)\notin\mathcal{R}(\mathbf{A}_u)$, the maximum number of interested lags for ZCZ, i.e., $L_A$, also must be reduced. Likewise, the

enhanced GMF design for the scenario with multiple transmit sequences can be formulated by minimizing $U$ GMFs' energy, i.e.,

$$\mathbf{S}^{\star} = \arg\min_{\mathbf{s}_u \in \mathcal{S}} \sum_{u=1}^{U} \mathbf{s}_u^H \mathbf{P}_{\mathbf{A}_u} \mathbf{s}_u, \ \mathbf{p}_u^{\star} = \mathbf{E}_{\mathbf{s}_u^{\star}|\mathbf{A}_u^{\star}}^H \mathbf{s}_u^{\star}. \tag{48}$$

*Remark 1:* Although the proposed GMF is designed within the specific context of radar target detection, its fundamental principle: leveraging oblique projection to achieve a ZCZ for transmit sequences, offers wide applicability. On this basis, the proposed method can also be naturally extended to other applications that rely on MF while seeking to mitigate sequence correlation interference, including sonar systems, navigation systems, code division multiple access communication systems, medical imaging, and other related fields.

## V. Numerical Results

In this section, we conduct representative simulations to examine the range sidelobe suppression and range resolution performance of the proposed GMF. It is demonstrated that the GMF can achieve a ZCZ, for comparison, we benchmark our method against the transmit design method in [29] and the transceiver design method in [42]. Similarly, both methods consider constant modulus constraint for sequence design. Unless specified otherwise, the transmit sequence is initialized to a random phase sequence $\mathbf{s}^{(0)}$, the sequence length is set to $L = 100$, and all subsequent simulations are conducted using the same sequence $\mathbf{s}^{(0)}$. The interested lags are set to $\Omega_s^{\|} = \{\pm 1, \pm 2, \cdots, \pm \frac{L_A}{2}\}$ with $L_A = 98$. The number of discrete phases and the convergence threshold of the enhanced GMF are set to $M = 100$ and $\xi = 10^{-3}$, respectively.

### A. ACF Performance of GMF

In this subsection, we validate the ACF performance of the GMF shown in (16). Fig. 4 provides the normalized ACF level (i.e., $20\log_{10}\frac{|\chi_{\mathbf{s},\mathbf{p}}(k)|}{L}$) using GMF for different cases and compares it to the MF, where Case 1: the interested lags are set to $\Omega_s^{\|} = \{\pm 1, \pm 2, \cdots, \pm 49\}$, Case 2: the interested lags are set to $\Omega_s^{\|} = \{\pm 1, \pm 2, \cdots, \pm 25\} \cup \{\pm 50, \pm 51, \cdots, \pm 73\}$. Compared with the MF, we can see from Fig. 4 that GMF creates the specified ZCZ at the interested lags in both cases while ensuring the peak correlation level without loss. However, for GMF, the correlation sidelobes at uninterested lags are higher than those of MF. Since the construction process of GMF involves matrix inversion, numerical calculation errors cause the ZCZ results not to be strictly equal to 0. Due to this unavoidable factor, the GMF energy also impacts the ZCZ performance, as evidenced by the following simulations. Importantly, due to the construction mechanism of GMF, the peak correlation level remains unaffected.

To assess the ACF performance of GMF under different transmit sequences, we consider the classical LFM signal and the random frequency modulation (RFM) signal [46]. The signal time width and bandwidth are set to 1 $\mu$s and 50 MHz, respectively, and the sampling frequency is 100 MHz. Moreover,

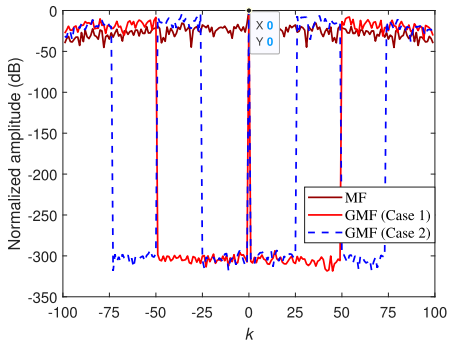


Fig. 4. The normalized ACF performance comparison of using the MF and the GMF with different ZCZs.

TABLE II
The ACF Performance of Using GMF for Various Sequences

| Sequence | Peak level (dB) | Average level (dB) at interested lags | Average level (dB) at uninterested lags |
|---|---|---|---|
| LFM | 0 | -202.60 | 10.66 |
| RFM ($\tilde{F} = 30$) | 0 | -272.97 | -13.86 |
| RFM ($\tilde{F} = 60$) | 0 | -285.35 | -16.79 |

TABLE III
The GMF Energy Corresponding to Various Transmit Sequences

| Sequence | GMF energy |
|---|---|
| LFM | 283240.58 |
| RFM ($\tilde{F} = 30$) | 14894.99 |
| RFM ($\tilde{F} = 60$) | 3917.67 |

for the RFM signal, the interval of the uniform distribution of the Fourier coefficients is set to $[-0.1, 0.1]$, and we consider two cases with random Fourier coefficient counts $\tilde{F} = 30$ and $\tilde{F} = 60$, representing different degrees of randomness. Table II provides normalized ACF levels (peak level, average level at interested and uninterested lags) of using GMF for various sequences. From Table II, we can see that the GMF can maintain the peak level without loss while achieving a ZCZ for various sequences. It is important to note that the GMF exhibits relatively high correlation level for the LFM signal. However, as the randomness of the sequence increases, the correlation level decreases accordingly, i.e., for the RFM signal with a larger $\tilde{F}$. This is because the GMF energy under various sequences is different, as presented in Table III. From Table III, we can see that a lower degree of sequence randomness results in higher GMF energy, thus elevating the correlation level at both interested and uninterested lags.

To demonstrate the impact of $L_A$ on the ACF performance of GMF, Fig. 5(a) shows the normalized ACF level using GMF with different $L_A$ and compares it to the MF. As we can see from Fig. 5(a), for GMF, the peak correlation level remains without loss with different $L_A$, $\chi_{\mathbf{s}^{(0)},\mathbf{p}^{(0)}}(k) \approx 0$ at interested lags, and correlation sidelobes at uninterested lags are comparable to that of the MF when $L_A$ is relatively small. The correlation sidelobe level increases when $L_A = 98$, this is because

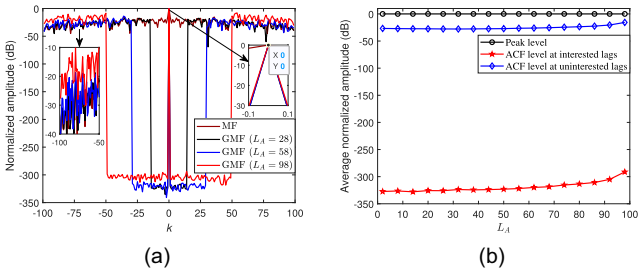


Fig. 5. (a) The normalized ACF performance comparison of using the MF and the GMF with different $L_A$. (b) The average normalized ACF level of using GMF under varying $L_A$ within different lag regions.

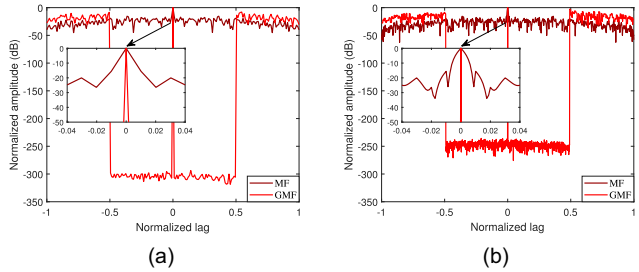


Fig. 6. The range resolution comparison of using the MF and GMF without noise. (a) Case of no increase in sampling frequency: $\varsigma = 1$. (b) Case of increased sampling frequency: $\varsigma = 8$.

a larger $L_A$ results in a smaller-dimensional subspace $\mathcal{R}^{\perp}(\mathbf{A})$ and a larger $\mathbf{s}^H\mathbf{P}_{\mathbf{A}}\mathbf{s}$, which increases the GMF energy and consequently elevates the correlation sidelobe level. To verify this, Fig. 5(b) depicts the normalized ACF levels (peak level, average level at interested and uninterested lags) of using GMF under varying $L_A$. From Fig. 5(b), it is evident that the peak level remains without loss, and the correlation sidelobe level increases as $L_A$ increases.

### *B. Range Resolution Performance of GMF*

To confirm the high range resolution advantage of the proposed GMF, Fig. 6 compares the normalized ACF performance of using MF and GMF in different sampling frequency scale factors, i.e., $\varsigma = 1$ and $\varsigma = 8$, respectively. To facilitate the comparison of the lag region of interest under different sampling frequencies, the lag axis has been normalized. As analyzed in Section III-B, to approximately keep the same lag region of interest under varying sampling frequencies, we set $L_{\breve{A}} = \varsigma L_A$. From Fig. 6, we observe that GMF yields a higher range resolution than that of MF in both cases. Besides, as $\varsigma$ increases, the mainlobe response using the MF becomes more "distinct", but this improvement does not enhance the range resolution due to fixed signal bandwidth $B_s$, i.e., $L$ is not increased with $\varsigma$. In contrast, by employing GMF, the range resolution improves as $\varsigma$ increases. However, its ZCZ performance degrades, and correlation sidelobes at uninterested lags elevate. As stated in Section III-D, this deterioration occurs because the relative GMF energy increases w.r.t. $\varsigma$, resulting in an elevated correlation level.

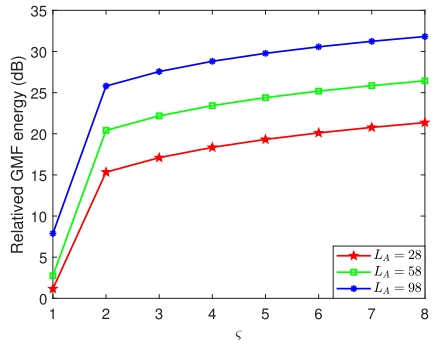


Fig. 7. Relative GMF energy versus sampling frequency scale factor $\varsigma$ under the different lag ranges of interest $L_A$.

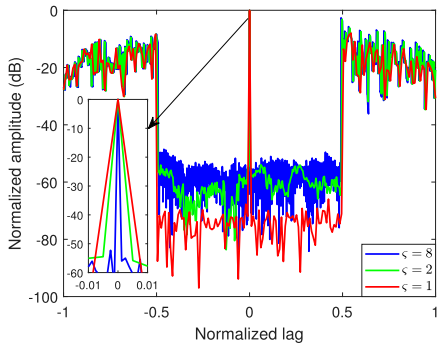


Fig. 8. Range resolution performance of using GMF under different sampling frequency scale factors $\varsigma$ when considering noise.

To validate the analysis in Section III-D, Fig. 7 depicts the relative GMF energy versus different sampling frequency scale factors $\varsigma$ under various lag ranges of interest $L_A$. For a fixed $L_A$, it is clear that as $\varsigma$ increases, the relative GMF energy increases, supporting the conclusion drawn in Section III-D. For different $L_A$, we can see that a larger $L_A$ leads to a larger relative GMF energy. To demonstrate the impact of increased frequency on the output SNR of GMF, we further evaluate its range resolution performance in the presence of noise. Fig. 8 shows the normalized ACF of using GMF under different $\varsigma$, with additive noise at a level of -60 dB. The noise is modeled as a zero-mean circularly symmetric complex Gaussian random vector. It is evident that the higher range resolution can be achieved by increasing $\varsigma$. However, since the relative GMF energy increases with $\varsigma$, a larger value of $\varsigma$ leads to higher output noise power, resulting in degraded output SNR performance. The above analyses and simulations clearly demonstrate that high range resolution can be achieved within the GMF framework. Nevertheless, it should be noted that high range resolution performance comes at the cost of other performance metrics.

### *C. ACF Performance of Enhanced GMF*

Building on the previous analysis, the GMF can establish a ZCZ while preserving the peak correlation level without loss. Additionally, it is compatible with various transmit sequences and exhibits high range resolution. However, its energy is uncontrolled, leading to high ACF levels at uninterested lags and

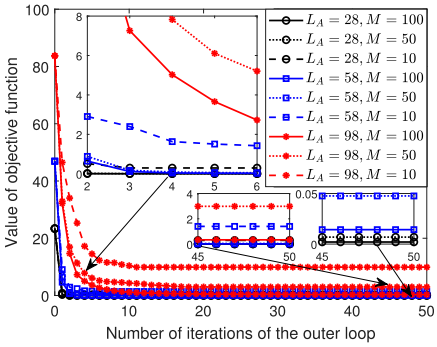


Fig. 9. Value of objective function $\mathbf{s}^H\mathbf{P_A}\mathbf{s}$ versus the number of iterations with different $L_A$ and $M$.

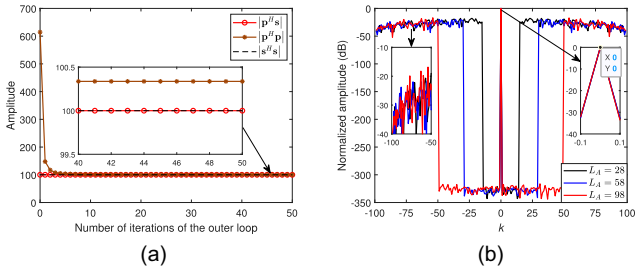


Fig. 10. (a) The convergence performance of the enhanced GMF. (b) The normalized ACF performance of using the enhanced GMF with different $L_A$.

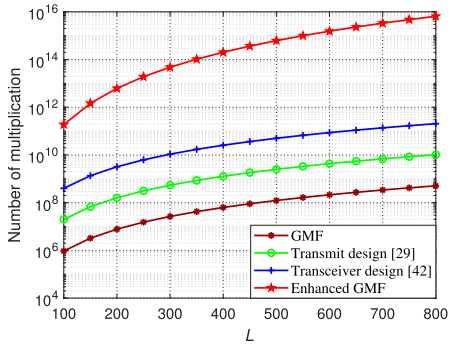


Fig. 11. The design complexity comparison of different methods.

the loss of output SNR. In this subsection, we assess the ACF performance of the enhanced GMF presented in (41). Firstly, we compare the convergence performance of our sequence design method for the enhanced GMF with different $L_A$ and $M$. Fig. 9 shows curves of the objective function value $\mathbf{s}^H\mathbf{P_A}\mathbf{s}$ versus the iteration number. As can be seen from Fig. 9, for the same $M$, the initial (ultimate) objective function value decreases as $L_A$ decreases. For the same $L_A$, the objective function value converges to a smaller value as $M$ increases, as larger $M$ provides more degrees of freedom for sequence design. It is important to note that even if $L_A$ is large (i.e., $L_A = 98$), we can design $\mathbf{s}$ to lead $\mathbf{s}^H\mathbf{P_A}\mathbf{s} \to 0$, thereby controlling the GMF energy and achieving output SNR loss $\to 0$ under the white noise assumption.

To proceed, Fig. 10(a) shows the convergence performance of the enhanced GMF. As the iteration number increases, we can see that the peak correlation level $\left|\mathbf{p}^H\mathbf{s}\right|$ of using enhanced GMF consistently aligns with $\left|\mathbf{s}^H\mathbf{s}\right|$ that of using the MF. From Fig. 9, since the objective function value $\mathbf{s}^H\mathbf{P_A}\mathbf{s}$ decreases as the iteration number increases, the energy $\left|\mathbf{p}^H\mathbf{p}\right|$ of the enhanced GMF gradually converges to the energy $\left|\mathbf{s}^H\mathbf{s}\right|$ of the MF. Thereby, the output amplitude for undesired signals can be controlled by leveraging the enhanced GMF. Fig. 10(b) provides the normalized ACF level of using the enhanced GMF with different $L_A$. From Fig. 10(b), using optimized sequence $\mathbf{s}^\star$ and enhanced GMF $\mathbf{p}^\star$, the GMF energy is minimized thus the ACF level at uninterested lags decreases compared to that in Fig. 5, especially for $L_A = 98$. It is important to note that $\mathbf{s}^\star$ and $\mathbf{p}^\star$ are individually designed for different $L_A$. Thereby, the ACF level at uninterested lags will not change significantly as $L_A$ increases.

### D. ACF and Complexity Comparison With Various Methods

In this subsection, we compare the proposed method with transmit design method [29] and transceiver design method [42]. Firstly, we assess the design complexity of various methods. For transmit design method [29], we know that its computational complexity is $\mathcal{O}(N_t L^3)$. For transceiver design method [42], its complexity is $\mathcal{O}(N_t N_{t,i} L^3)$, where $N_t$ and $N_{t,i}$ denote the iteration number of the outer loop and inner loop, respectively. We set $N_t = N_{t,i} = 20$, $M = L$, and $L_A = L - 2$, Fig. 11 compares the design complexity of different methods under varying $L$. The simulation results reveal that the design complexity of each method increases with $L$. The GMF has the lowest design complexity, while the enhanced GMF has the highest. Notably, the design complexity of the enhanced GMF relies on the specific enhancement (sequence design) method used. To further assess the real-time feasibility of the proposed method, Table IV compares the offline design time versus online PC time for GMF, enhanced GMF, and standard MF. The simulations are conducted on the same software (MATLAB R2021b) and hardware configuration: CPU: Intel Core i7-10700 at 2.90 GHz; RAM: 32 GB. As shown in Table IV, the offline design time of GMF is negligible, whereas that of enhanced GMF is the longest. The online PC times of GMF, enhanced GMF, and standard GMF are comparable and can be efficiently implemented using the FFT, confirming the real-time capability of the proposed method. Although the enhanced GMF introduces greater design complexity, it can be well-designed offline and subsequently perform PC online in the same manner as the MF. Developing more efficient design approaches for the enhanced GMF is a valuable topic for future research, but lies beyond the scope of this work.

TABLE IV
COMPARISON OF OFFLINE DESIGN TIME VERSUS ONLINE PC TIME FOR GMF, ENHANCED GMF, AND STANDARD MF

| | GMF | Enhanced GMF | Standard MF |
|---|---|---|---|
| Offline design time (s) | $4.53 \times 10^{-4}$ | 858.98 | - |
| Online PC time (s) | $0.56 \times 10^{-5}$ | $0.47 \times 10^{-5}$ | $1.45 \times 10^{-5}$ |

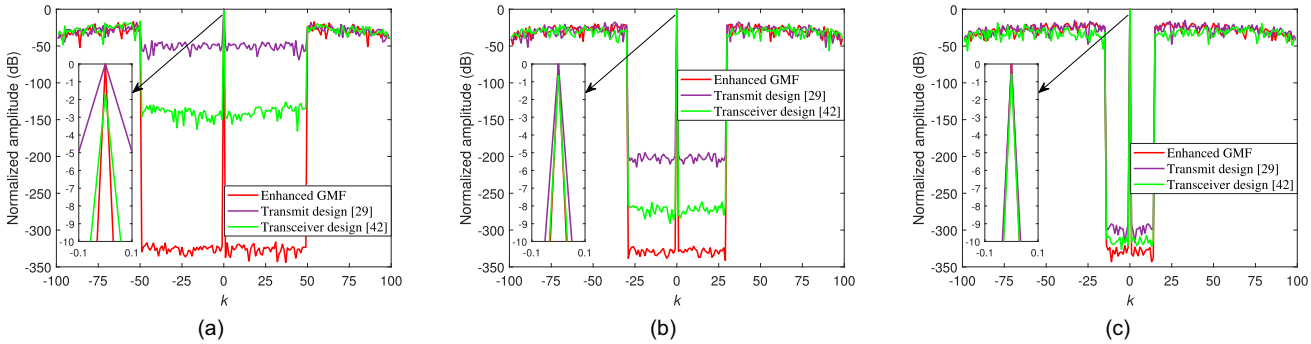


Fig. 12. The normalized ACF performance comparison of different methods with varying $L_A$. (a) $L_A = 98$. (b) $L_A = 58$. (c) $L_A = 28$.

Subsequently, Fig. 12 compares the ACF performance of different methods. It is evident that three methods can achieve low ACF levels at interested lags. When $L_A = 98$, for transmit design method [29], the ZCZ performance is limited, but there is no loss in peak correlation level. For transceiver design method [42], the ZCZ performance is improved compared to transmit design method [29], but there is a peak correlation level loss of approximately 2 dB. As $L_A$ decreases, the ZCZ performance of transmit design method [29] and transceiver design method [42] is improved, and the peak correlation level loss of transceiver design method [42] is reduced. The ACF level at uninterested lags with different $L_A$ of the three methods is comparable. In contrast, the proposed GMF not only maintains the peak correlation level without loss, but also achieves better ZCZ performance.

### *E. Target Range Profile Extraction Performance*

In this subsection, we compare the target range profile (TRP) extraction performance of different methods in the presence of noise. We set four targets, including two strong scatterers and two weak scatterers. The detailed target parameters are as follows: Target 1: [60, 10], Target 2: $[0, 20]$, Target 3: [60, 30], Target 4: $[0, 40]$, where the data format of each target is represented as [SNR (dB), index of range cell].

To assess the TRP extraction performance of our method, Fig. 13 presents the extracted TRPs by the MF, GMF, and enhanced GMF, respectively, where the normalized amplitude refers to scaling the output by normalizing it relative to the maximum output value. As we can see from Fig. 13, by employing the MF $\mathbf{s}^{(0)}$, two weak targets are obscured in the range sidelobes of the stronger. By using the GMF $\mathbf{p}^{(0)}$, four TRPs can all be extracted, but the output amplitude at uninterested regions is relatively large and the output SNR gain of two weak scatters is relatively low, i.e., 15.46 dB, where the output SNR gain is calculated by the ratio of the target output power to the sum of the output powers of the 1∼59th range cells excluding 4 target range cells. By using optimized sequence $\mathbf{s}^\star$ and enhanced GMF $\mathbf{p}^\star$, the output range sidelobes at uninterested lags are decreased, and the output SNR gain is improved. With the analysis in Section V-C, the enhanced GMF can lead to output SNR loss $\to 0$, thus the output SNR gain of the enhanced GMF approximately equal to theoretical output SNR gain $10\log_{10} L = 20$ dB.

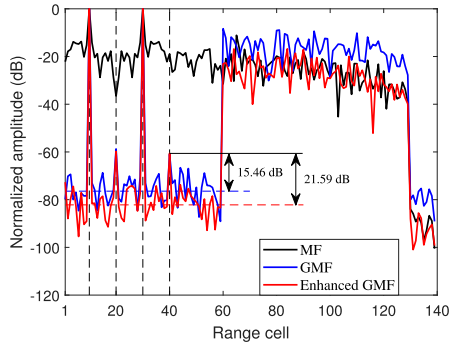


Fig. 13. The TRP extraction performance comparison of using the MF, the GMF, and the enhanced GMF.

Ultimately, Fig. 14(a) and 14(b) compare the TRP extraction performance of various methods in different target scenarios. In Scenario 1, the target parameters are identical to that in the previous experiment, i.e., Target 1: [60, 10], Target 2: $[0, 20]$, Target 3: [60, 30], Target 4: $[0, 40]$. In Scenario 2, the target parameters are set as follows: Target 1: $[150, 10]$, Target 2: $[0, 20]$, Target 3: $[150, 30]$, Target 4: $[0, 40]$. As can be seen from Fig. 14(a), transmit design method [29] can only extract two strong TRPs. Both transceiver design method [42] and the proposed GMF can extract four TRPs. Since the output SNR loss of transceiver design method [42] is greater than that of our method, the output SNR gain of transceiver design method [42] is about 2.07 dB less than that of the proposed method. As we can see from Fig. 14(b), when the SNR of two strong scatterers increases to 150 dB, transceiver design method [42] can no longer extract two weak TRPs due to the high range sidelobes of the stronger. As expected, only the proposed GMF can effectively suppress the range sidelobes and precisely extract four TRPs. The above simulation results clearly demonstrate the effectiveness and superiority of the proposed GMF.

## VI. Conclusion

In this paper, we have presented a GMF framework leveraging oblique projection for range sidelobe suppression. For a given transmit sequence, the GMF is derived as a closed form. The designed GMF flexibly achieves a specified ZCZ while maintaining the peak correlation level without loss. Moreover, it is compatible with various transmit sequences and provides

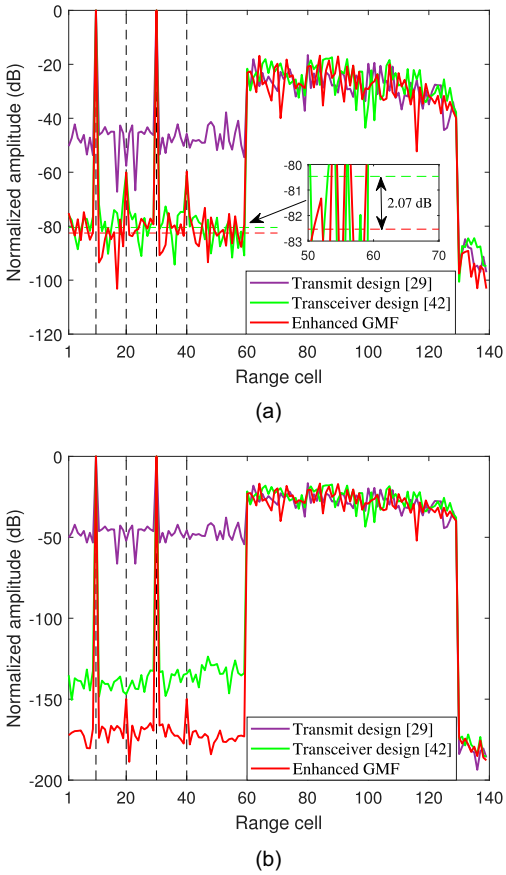


Fig. 14. The TRP extraction performance comparison of different methods. (a) Scenario 1. (b) Scenario 2.

higher range resolution, exhibiting a distinct advantage over the standard MF. The GMF can be well-designed offline and then implemented online for pulse compression. It provides greater efficiency than existing online signal processing methods. We have conducted a comprehensive performance analysis of GMF, and have presented the distinctions and connections between GMF and MF. The cost introduced by high range resolution within the GMF framework has been explored. In addition, we have presented an enhanced GMF by optimizing the transmit sequence, which can effectively mitigate the range profile masking problem while achieving negligible output SNR loss. Furthermore, we have investigated several extended applications of the GMF. Representative simulations have been presented to validate the effectiveness and superiority of the proposed GMF framework.

## APPENDIX A
## PROOF OF PROPOSITION 1

For the sake of clarity and illustration, the specific form of $\widetilde{\mathbf{A}}$ is presented in (49) at the bottom of this page.

For Case 1, we have $\tilde{\Omega}_s^{\|} = \{-L+1, -L+2, \cdots, -1\}$. In this case, the matrix consists of $L-1$ time shifted versions of $\mathbf{s}$ can be denoted as:

$$\mathbf{B} = [\mathbf{J}_{-L+1}\mathbf{s}, \mathbf{J}_{-L+2}\mathbf{s}, \cdots, \mathbf{J}_{-1}\mathbf{s}] \in \mathbb{C}^{L\times(L-1)}. \tag{50}$$

Denote $\mathbf{b}_i \in \mathbb{C}^L$ the $i$th column vector of $\mathbf{B}$, $i = 1, 2, \cdots, L-1$, expressed as:

$$\mathbf{b}_i = [\underbrace{0, \cdots, 0}_{L-i \text{ zeros}}, s(1), s(2), \cdots, s(i)]^T. \tag{51}$$

According to (49) and (51), we can see that $\mathbf{B}$ is composed of the first $L-1$ column vectors of $\widetilde{\mathbf{A}}$. Let $\widetilde{\mathbf{B}} = [\mathbf{B}, \mathbf{s}] \in \mathbb{C}^{L\times L}$, it is evident that $\widetilde{\mathbf{B}}$ is a triangular matrix. Since $\forall l, s(l) \neq 0$, we have

$$|\widetilde{\mathbf{B}}| = [s(1)]^L \neq 0. \tag{52}$$

Therefore, $\widetilde{\mathbf{B}}$ has a full column rank and $\mathcal{R}(\mathbf{s}) \notin \mathcal{R}(\mathbf{B})$. On this basis, if the interested lags $\Omega_s^{\|} \subseteq \tilde{\Omega}_s^{\|}$, i.e., select $L_A$ column vectors from $\mathbf{B}$ to construct $\mathbf{A}$, $\mathbf{s} \notin \mathcal{R}(\mathbf{A})$ is guaranteed to hold, independent of the specific form of $\mathbf{s}$.

Similarly, for Case 2, we have $\tilde{\Omega}_s^{\|} = \{1, 2, \cdots, L-1\}$. In this case, the matrix consists of $L-1$ time shifted versions of $\mathbf{s}$ can be denoted as:

$$\mathbf{C} = [\mathbf{J}_1\mathbf{s}, \mathbf{J}_2\mathbf{s}, \cdots, \mathbf{J}_{L-1}\mathbf{s}] \in \mathbb{C}^{L\times(L-1)}. \tag{53}$$

Denote $\mathbf{c}_j \in \mathbb{C}^L$ the $j$th column vector of $\mathbf{C}$, $j = 1, 2, \cdots, L-1$, given by:

$$\mathbf{c}_j = [s(j+1), \cdots, s(L), \underbrace{0, \cdots, 0}_{j \text{ zeros}}]^T. \tag{54}$$

According to (49) and (54), we can see that $\mathbf{C}$ is composed of the last $L-1$ column vectors of $\widetilde{\mathbf{A}}$. Let $\widetilde{\mathbf{C}} = [\mathbf{s}, \mathbf{C}] \in \mathbb{C}^{L\times L}$, it is evident that $\widetilde{\mathbf{C}}$ is also a triangular matrix, we have

$$|\widetilde{\mathbf{C}}| = [s(L)]^L \neq 0. \tag{55}$$

$\widetilde{\mathbf{C}}$ has a full column rank and $\mathcal{R}(\mathbf{s}) \notin \mathcal{R}(\mathbf{C})$. On this basis, if the interested lags $\Omega_s^{\|} \subseteq \tilde{\Omega}_s^{\|}$, i.e., select $L_A$ column vectors from $\mathbf{C}$ to construct $\mathbf{A}$, $\mathbf{s} \notin \mathcal{R}(\mathbf{A})$ is guaranteed to hold, independent of the specific form of $\mathbf{s}$.

For Case 3, we know that

$$\tilde{\Omega}_s^{\|} = \{-L+1, -L+2, \cdots, -l\}$$

$$\widetilde{\mathbf{A}} = \begin{bmatrix} 0 & \cdots & 0 & 0 & 0 & s(2) & s(3) & s(4) & \cdots & s(L) \\ 0 & \cdots & 0 & 0 & s(1) & \vdots & \vdots & \vdots & \iddots & \vdots \\ 0 & \cdots & 0 & s(1) & s(2) & s(L-2) & s(L-1) & s(L) & \cdots & 0 \\ 0 & \cdots & s(1) & s(2) & s(3) & s(L-1) & s(L) & 0 & \cdots & 0 \\ \vdots & \iddots & \vdots & \vdots & \vdots & s(L) & 0 & 0 & \cdots & 0 \\ s(1) & \cdots & s(L-3) & s(L-2) & s(L-1) & 0 & 0 & 0 & \cdots & 0 \end{bmatrix} \in \mathbb{C}^{L\times(2L-2)}. \tag{49}$$

$$\cup \{L-l+1, L-l+2, \cdots, L-1\} \tag{56}$$

where $2 \le l \le L-1$. In this case, the matrix consists of $L-1$ time shifted versions of $\mathbf{s}$ can be denoted as:

$$\mathbf{D}_1 = [\mathbf{J}_{-L+1}\mathbf{s}, \mathbf{J}_{-L+2}\mathbf{s}, \cdots, \mathbf{J}_{-l}\mathbf{s}] \in \mathbb{C}^{L\times(L-l)} \tag{57a}$$

$$\mathbf{D}_2 = [\mathbf{J}_{L-l+1}\mathbf{s}, \mathbf{J}_{L-l+2}\mathbf{s}, \cdots, \mathbf{J}_{L-1}\mathbf{s}] \in \mathbb{C}^{L\times(l-1)} \tag{57b}$$

$$\mathbf{D} = [\mathbf{D}_1, \mathbf{D}_2] \in \mathbb{C}^{L\times(L-1)}. \tag{57c}$$

According to (50) and (53), we can see that $\mathbf{D}$ is composed of the first $L-l$ column vectors of $\mathbf{B}$ and last $l-1$ column vectors of $\mathbf{C}$, it follows that both $\mathbf{D}_1$ and $\mathbf{D}_2$ have full column rank. From (51), we can find that the nonzero elements of $\mathbf{D}_1$ are located in rows $l+1 \sim L$. From (54), we can find that the nonzero elements of $\mathbf{D}_2$ are located in rows $1 \sim l-1$. On this basis, we have

$$\mathbf{D}_{l,:} = \mathbf{0}_{L-1}^T,\ 2 \le l \le L-1. \tag{58}$$

Let $\widetilde{\mathbf{D}} = [\mathbf{s}, \mathbf{D}] \in^{L\times L}$, we now proceed to analyze the rank of $\widetilde{\mathbf{D}}$. This is equivalent to examining whether there exists a set of coefficients $\{x_p\}_{p=1}^{L}$ not all zero, such that the following equation holds:

$$\begin{aligned} &x_1\mathbf{s} + x_2\mathbf{J}_{-L+1}\mathbf{s} + \cdots + x_p\mathbf{J}_{-l}\mathbf{s} \\ &\quad + x_{p+1}\mathbf{J}_{L-l+1}\mathbf{s} + \cdots + x_L\mathbf{J}_{L-1}\mathbf{s} = \mathbf{0}_L. \end{aligned} \tag{59}$$

According to (58), we have

$$\widetilde{\mathbf{D}}_{l,:} = [s(l), \mathbf{0}_{L-1}^T],\ 2 \le l \le L-1. \tag{60}$$

On this basis, it is evident that

$$x_1 = 0. \tag{61}$$

Exploiting the structure of matrices $\mathbf{D}_1$ and $\mathbf{D}_2$, we can convert (59) into the following two equations:

$$x_2\mathbf{J}_{-L+1}\mathbf{s} + \cdots + x_p\mathbf{J}_{-l}\mathbf{s} = \mathbf{0}_L \tag{62a}$$

$$x_{p+1}\mathbf{J}_{L-l+1}\mathbf{s} + \cdots + x_L\mathbf{J}_{L-1}\mathbf{s} = \mathbf{0}_L. \tag{62b}$$

Since both $\mathbf{D}_1$ and $\mathbf{D}_2$ have full column rank, we have

$$x_2 = x_3 = \cdots = x_p = 0 \tag{63a}$$

$$x_p = x_{p+1} = \cdots = x_L = 0. \tag{63b}$$

According to (61) and (63), $\widetilde{\mathbf{D}}$ has a full column rank and $\mathcal{R}(\mathbf{s}) \notin \mathcal{R}(\mathbf{D})$. As a result, if the interested lags $\Omega_s^{\|} \subseteq \tilde{\Omega}_s^{\|}$, i.e., select $L_A$ column vectors from $\mathbf{D}$ to construct $\mathbf{A}$, $\mathbf{s} \notin \mathcal{R}(\mathbf{A})$ is guaranteed to hold, independent of the specific form of $\mathbf{s}$.

This completes the proof.

## Appendix B
## Proof of Proposition 2

From (1), the projection of oblique projector $\mathbf{E}_{\mathbf{s}|\mathbf{A}}$ on any vector $\mathbf{a}$ can be expressed as

$$\mathbf{E}_{\mathbf{s}|\mathbf{A}}\mathbf{a} = \mathbf{s}(\mathbf{s}^H\mathbf{P}_{\mathbf{A}}^{\perp}\mathbf{s})^{-1}\mathbf{s}^H\mathbf{P}_{\mathbf{A}}^{\perp}\mathbf{a} = \mathbf{s}\beta \tag{64}$$

where $\beta = (\mathbf{s}^H\mathbf{P}_{\mathbf{A}}^{\perp}\mathbf{s})^{-1}\mathbf{s}^H\mathbf{P}_{\mathbf{A}}^{\perp}\mathbf{a}$.

Let $\mathbf{a} = \tilde{\mathbf{a}}\|\mathbf{a}\|_2$, where $\tilde{\mathbf{a}}$ denotes the normalized vector of $\mathbf{a}$. It is well known that orthogonal projector $\mathbf{P}_{\mathbf{A}}^{\perp}$ is a positive semidefinite Hermite matrix, thus we have

$$|\beta| = \frac{|\mathbf{s}^H\mathbf{P}_{\mathbf{A}}^{\perp}\mathbf{a}|}{\mathbf{s}^H\mathbf{P}_{\mathbf{A}}^{\perp}\mathbf{s}} = \|\mathbf{a}\|_2 \frac{|\mathbf{s}^H\mathbf{P}_{\mathbf{A}}^{\perp}\tilde{\mathbf{a}}|}{\left\|(\mathbf{P}_{\mathbf{A}}^{\perp})^{\frac{1}{2}}\mathbf{s}\right\|_2^2}. \tag{65}$$

Leveraging the Cauchy-Schwarz inequality, the numerator in (65) owns the following relationship:

$$\begin{aligned} |\mathbf{s}^H\mathbf{P}_{\mathbf{A}}^{\perp}\tilde{\mathbf{a}}| &= \left|\mathbf{s}^H(\mathbf{P}_{\mathbf{A}}^{\perp})^{\frac{1}{2}}(\mathbf{P}_{\mathbf{A}}^{\perp})^{\frac{1}{2}}\tilde{\mathbf{a}}\right| \\ &\le \left\|(\mathbf{P}_{\mathbf{A}}^{\perp})^{\frac{1}{2}}\mathbf{s}\right\|_2 \left\|(\mathbf{P}_{\mathbf{A}}^{\perp})^{\frac{1}{2}}\tilde{\mathbf{a}}\right\|_2. \end{aligned} \tag{66}$$

Since $\tilde{\mathbf{a}}$ is the normalized vector of $\mathbf{a}$, $\tilde{\mathbf{a}}^H\tilde{\mathbf{a}} = 1$, we have

$$\left\|(\mathbf{P}_{\mathbf{A}}^{\perp})^{\frac{1}{2}}\tilde{\mathbf{a}}\right\|_2 = \sqrt{\tilde{\mathbf{a}}^H\mathbf{P}_{\mathbf{A}}^{\perp}\tilde{\mathbf{a}}}\Big|_{\tilde{\mathbf{a}}^H\tilde{\mathbf{a}}=1} \le \sqrt{\lambda_{\max}(\mathbf{P}_{\mathbf{A}}^{\perp})}. \tag{67}$$

Using the fact that the eigenvalues of an orthogonal projection matrix are either 1 or 0. Thereby, we have

$$\lambda_{\max}(\mathbf{P}_{\mathbf{A}}^{\perp}) = 1 \tag{68}$$

and (67) can be recast as

$$\left\|(\mathbf{P}_{\mathbf{A}}^{\perp})^{\frac{1}{2}}\tilde{\mathbf{a}}\right\|_2 \le 1. \tag{69}$$

Substituting (66) and (69) into (65), the value range of $|\beta|$ can be obtained as

$$0 \le |\beta| \le \frac{\|\mathbf{a}\|_2}{\left\|(\mathbf{P}_{\mathbf{A}}^{\perp})^{\frac{1}{2}}\mathbf{s}\right\|_2} = \|\mathbf{a}\|_2(\mathbf{s}^H\mathbf{s} - \mathbf{s}^H\mathbf{P}_{\mathbf{A}}\mathbf{s})^{-\frac{1}{2}}. \tag{70}$$

From (13), we know that $\mathbf{s}^H\mathbf{P}_{\mathbf{A}}\mathbf{s} < \mathbf{s}^H\mathbf{s}$ is the prerequisite for (14) to hold. Thereby, we can obtain that $\mathbf{s}^H\mathbf{s} - \mathbf{s}^H\mathbf{P}_{\mathbf{A}}\mathbf{s} > 0$ holds and the upper bound in (70) is finite and reasonable.

Combining (16) and (70), the filtering output amplitude of $\mathbf{p}$ for signal $\mathbf{a}$ satisfies

$$\begin{aligned} 0 \le |\mathbf{p}^H\mathbf{a}| &= |\mathbf{s}^H\mathbf{E}_{\mathbf{s}|\mathbf{A}}\mathbf{a}| = |\beta|\,\mathbf{s}^H\mathbf{s} \\ &\le \|\mathbf{a}\|_2 \underbrace{\mathbf{s}^H\mathbf{s}(\mathbf{s}^H\mathbf{s} - \mathbf{s}^H\mathbf{P}_{\mathbf{A}}\mathbf{s})^{-\frac{1}{2}}}_{=\|\mathbf{p}\|_2}. \end{aligned} \tag{71}$$

This completes the proof.

## References


[1] M. A. Richards, *Fundamentals of Radar Signal Processing*, vol. 1. New York, NY, USA: McGraw-Hill, 2005.

[2] S. D. Blunt and E. L. Mokole, "Overview of radar waveform diversity," *IEEE Aerosp. Electron. Syst. Mag.*, vol. 31, no. 11, pp. 2–42, Nov. 2016.

[3] A. Aubry, V. Carotenuto, A. De Maio, and L. Pallotta, "High range resolution profile estimation via a cognitive stepped frequency technique," *IEEE Trans. Aerosp. Electron. Syst.*, vol. 55, no. 1, pp. 444–458, Feb. 2019.

[4] M. H. Ackroyd and F. Ghani, "Optimum mismatched filters for sidelobe suppression," *IEEE Trans. Aerosp. Electron. Syst.*, no. 2, pp. 214–218, Mar. 1973.

[5] R. Sato and M. Shinrhu, "Simple mismatched filter for binary pulse compression code with small PSL and small S/N loss [radar]," *IEEE Trans. Aerosp. Electron. Syst.*, vol. 39, no. 2, pp. 711–718, Apr. 2003.

[6] R. Bose, A. Freedman, and B. D. Steinberg, "Sequence CLEAN: A modified deconvolution technique for microwave images of contiguous

targets," *IEEE Trans. Aerosp. Electron. Syst.*, vol. 38, no. 1, pp. 89–97, Jan. 2002.
[7] H. Deng, "Effective CLEAN algorithms for performance-enhanced detection of binary coding radar signals," *IEEE Trans. Signal Process.*, vol. 52, no. 1, pp. 72–78, Jan. 2004.
[8] S. D. Blunt and K. Gerlach, "Adaptive pulse compression via MMSE estimation," *IEEE Trans. Aerosp. Electron. Syst.*, vol. 42, no. 2, pp. 572–584, Apr. 2006.
[9] Z. Li, Y. Zhang, S. Wang, L. Li, and M. Mclinden, "Fast adaptive pulse compression based on matched filter outputs," *IEEE Trans. Aerosp. Electron. Syst.*, vol. 51, no. 1, pp. 548–564, Jan. 2015.
[10] P. M. McCormick, S. D. Blunt, and T. Higgins, "A gradient descent implementation of adaptive pulse compression," in *Proc. IEEE Int. Radar Conf.*, 2016, pp. 1–5.
[11] J. Pei, Y. Huang, J. Guan, M. Cai, B. Chen, and X. Chen, "Robust adaptive pulse compression method based on two-stage phase compensation," *IEEE Trans. Geosci. Remote Sens.*, vol. 60, pp. 1–18, 2022.
[12] R. Barker, "Group synchronizing of binary digital systems," *in Communication Theory*. New York, NY, USA: Academic, 1953, pp. 273–287.
[13] P. Borwein and R. Ferguson, "Polyphase sequences with low autocorrelation," *IEEE Trans. Inf. Theory*, vol. 51, no. 4, pp. 1564–1567, Apr. 2005.
[14] C. J. Nunn and G. E. Coxson, "Polyphase pulse compression codes with optimal peak and integrated sidelobes," *IEEE Trans. Aerosp. Electron. Syst.*, vol. 45, no. 2, pp. 775–781, Apr. 2009.
[15] A. Pezeshki, A. R. Calderbank, W. Moran, and S. D. Howard, "Doppler resilient Golay complementary waveforms," *IEEE Trans. Inf. Theory*, vol. 54, no. 9, pp. 4254–4266, Sep. 2008.
[16] W. Dang, A. Pezeshki, S. Howard, W. Moran, and R. Calderbank, "Coordinating complementary waveforms for sidelobe suppression," in *Proc. 45st Asilomar Conf. Signals, Syst. Comput.*, 2011, pp. 2096–2100.
[17] Z.-J. Wu, C.-X. Wang, P.-H. Jiang, and Z.-Q. Zhou, "Range-Doppler sidelobe suppression for pulsed radar based on Golay complementary codes," *IEEE Signal Process. Lett.*, vol. 27, pp. 1205–1209, 2020.
[18] P. Stoica, H. He, and J. Li, "New algorithms for designing unimodular sequences with good correlation properties," *IEEE Trans. Signal Process.*, vol. 57, no. 4, pp. 1415–1425, Apr. 2009.
[19] J. Song, P. Babu, and D. P. Palomar, "Optimization methods for designing sequences with low autocorrelation sidelobes," *IEEE Trans. Signal Process.*, vol. 63, no. 15, pp. 3998–4009, Aug. 2015.
[20] J. Liang, H. C. So, C. S. Leung, J. Li, and A. Farina, "Waveform design with unit modulus and spectral shape constraints via Lagrange programming neural network," *IEEE J. Sel. Topics Signal Process.*, vol. 9, no. 8, pp. 1377–1386, Dec. 2015.
[21] J. Liang, H. C. So, J. Li, and A. Farina, "Unimodular sequence design based on alternating direction method of multipliers," *IEEE Trans. Signal Process*, vol. 64, no. 20, pp. 5367–5381, Oct. 2016.
[22] L. Zhao, J. Song, P. Babu, and D. P. Palomar, "A unified framework for low autocorrelation sequence design via majorization-minimization," *IEEE Trans. Signal Process.*, vol. 65, no. 2, pp. 438–453, Jan. 2017.
[23] M. A. Kerahroodi, A. Aubry, A. De Maio, M. M. Naghsh, and M. Modarres-Hashemi, "A coordinate-descent framework to design low PSL/ISL sequences," *IEEE Trans. Signal Process.*, vol. 65, no. 22, pp. 5942–5956, Nov. 2017.
[24] H. Torii, M. Nakamura, and N. Suehiro, "A new class of zero-correlation zone sequences," *IEEE Trans. Inf. Theory*, vol. 50, no. 3, pp. 559–565, Mar. 2004.
[25] J. Song, P. Babu, and D. P. Palomar, "Sequence design to minimize the weighted integrated and peak sidelobe levels," *IEEE Trans. Signal Process.*, vol. 64, no. 8, pp. 2051–2064, Apr. 2016.
[26] Y.-C. Wang, L. Dong, X. Xue, and K.-C. Yi, "On the design of constant modulus sequences with low correlation sidelobes levels," *IEEE Commun. Lett.*, vol. 16, no. 4, pp. 462–465, Apr. 2012.
[27] F-c Li, Y-n Zhao, and X-l Qiao, "A waveform design method for suppressing range sidelobes in desired intervals," *Signal Process*, vol. 96, pp. 203–211, Mar. 2014.
[28] G. Cui, X. Yu, Y. Yang, and L. Kong, "Cognitive phase-only sequence design with desired correlation and stopband properties," *IEEE Trans. Aerosp. Electron. Syst.*, vol. 53, no. 6, pp. 2924–2935, Dec. 2017.
[29] Z. Cheng, B. Liao, Z. He, J. Li, and C. Han, "A nonlinear-ADMM method for designing MIMO radar constant modulus waveform with low correlation sidelobes," *Signal Process.*, vol. 159, pp. 93–103, Jun. 2019.
[30] H. He, P. Stoica, and J. Li, "On aperiodic-correlation bounds," *IEEE Signal Process. Lett.*, vol. 17, no. 3, pp. 253–256, Mar. 2010.
[31] Y. Chen, Y. Cheng, R. Lin, H. C. So, and J. Li, "Joint design of binary probing sequence sets and receive filter banks for MIMO PMCW radar," *IEEE Trans. Signal Process.*, vol. 72, pp. 1620–1633, 2024.
[32] O. Rabaste and L. Savy, "Mismatched filter optimization for radar applications using quadratically constrained quadratic programs," *IEEE Trans. Aerosp. Electron. Syst.*, vol. 51, no. 4, pp. 3107–3122, Oct. 2015.
[33] P. J. Kajenski, "Mismatch filter design via convex optimization," *IEEE Trans. Aerosp. Electron. Syst.*, vol. 52, no. 4, pp. 1587–1591, Aug. 2016.
[34] Y. Sun, Q. Liu, J. Cai, and T. Long, "A novel weighted mismatched filter for reducing range sidelobes," *IEEE Trans. Aerosp. Electron. Syst.*, vol. 55, no. 3, pp. 1450–1460, Jun. 2019.
[35] M. Soltanalian, B. Tang, J. Li, and P. Stoica, "Joint design of the receive filter and transmit sequence for active sensing," *IEEE Signal Process. Lett.*, vol. 20, no. 5, pp. 423–426, May 2013.
[36] M. Alaee-Kerahroodi, L. Wu, E. Raei, and M. B. Shankar, "Joint waveform and receive filter design for pulse compression in weather radar systems," *IEEE Trans. Radar Syst.*, vol. 1, pp. 212–229, 2023.
[37] Z. Chen, J. Liang, T. Wang, B. Tang, and H. C. So, "Generalized MBI algorithm for designing sequence set and mismatched filter bank with ambiguity function constraints," *IEEE Trans. Signal Process.*, vol. 70, pp. 2918–2933, 2022.
[38] F. Wang, X.-G. Xia, C. Pang, X. Cheng, Y. Li, and X. Wang, "Joint design methods of unimodular sequences and receiving filters with good correlation properties and Doppler tolerance," *IEEE Trans. Geosci. Remote Sens.*, vol. 61, pp. 1–14, 2023.
[39] Y. Chen, R. Lin, Y. Cheng, and J. Li, "Joint design of periodic binary probing sequences and receive filters for PMCW radar," *IEEE Trans. Signal Process.*, vol. 70, pp. 5996–6010, 2022.
[40] Y. Chen, Z. Chen, Y. Zhang, J. Yang, and D. Li, "Joint design of Doppler resilient unimodular discrete phase sequence waveform and receiving filter for multichannel radar," *IEEE Trans. Signal Process.*, vol. 72, pp. 4207–4221, 2024.
[41] T. Wang, J. Liang, H. So, H. Gao, and Y. Li, "Designing sequence set and mismatched filter bank with diagonal-ridge-type Doppler tolerance via relative level optimization," *IEEE Trans. Signal Process.*, vol. 72, pp. 4412–4427, 2024.
[42] J. He, H. Li, Z. He, W. Wang, and Z. Cheng, "Exploiting base station for remote sensing: modeling, joint transceiver design, and experiment," *IEEE Trans. Aerosp. Electron. Syst.*, vol. 60, no. 6, pp. 8184–8197, Dec. 2024.
[43] Q. K. Trinh, P. Fan, D. Peng, and M. Darnell, "Construction of optimal mismatched periodic sequence sets with zero correlation zone," *IEEE Signal Process. Lett.*, vol. 15, pp. 341–344, 2008.
[44] R. T. Behrens and L. L. Scharf, "Signal processing applications of oblique projection operators," *IEEE Trans. Signal Process.*, vol. 42, no. 6, pp. 1413–1424, Jun. 1994.
[45] X. Zhang, Z. He, B. Liao, Y. Yang, J. Zhang, and X. Zhang, "Flexible array response control via oblique projection," *IEEE Trans. Signal Process.*, vol. 67, no. 12, pp. 3126–3139, Jun. 2019.
[46] Q. Xie, C. Liu, Z. Mo, and W. Li, "A novel pulse-agile waveform design based on random FM waveforms for range sidelobe suppression and range ambiguity mitigation," *IEEE Trans. Geosci. Remote Sens.*, vol. 61, pp. 1–12, 2023.

**Yalong Wang** (Graduate Student Member, IEEE) was born in Anhui, China, in 2000. He received the B.S. degree in communication engineering from the School of Information and Communication Engineering, North University of China (NUC), Taiyuan, China, in 2021. He is currently working toward the Ph.D. degree in information and communication engineering with the School of Information and Communication Engineering, University of Electronic Science and Technology of China (UESTC), Chengdu, China. His research interests include radar signal processing, space-time adaptive processing, and radar adaptive target detection.

**Xuejing Zhang** (Member, IEEE) was born in Hebei, China. He received the B.S. degree in electrical engineering from Huaqiao University, Xiamen, China, in 2011, the M.S. degree in signal and information processing from Xidian University, Xi'an, China, in 2014, and the Ph.D. degree in signal and information processing from the University of Electronic Science and Technology of China (UESTC), Chengdu, China, in 2019. From 2017 to 2019, he was a Visiting Student with the University of Delaware, Newark, DE, USA. He is currently an Associate Professor with the School of Information and Communication Engineering, UESTC. His research interests include array signal processing and integer programming, with applications to radar and communications. He was awarded the Young Scientists Award for Excellence in Scientific Research by the International Union of Radio Science (URSI) in 2020. He received the Prize for Excellent Doctor Degree Dissertation of the Chinese Institute of Electronics in 2020.

**Jinyang He** received the B.S. degree in information engineering from the Nanjing University of Aeronautics and Astronautics (NUAA), Nanjing, China, in 2019, and the Ph.D. degree in signal and information processing from the University of Electronic Science and Technology of China (UESTC), Chengdu, China, in 2025. He is currently a member of the Technical Staff with the AVIC Leihua Electronic Technology Research Institute, Wuxi, China. His research interests include radar waveform design and signal processing.

**Jun Li** was born in Sichuan, China, in 1977. He received the B.S., M.S., and Ph.D. degrees in signal and information processing from the University of Electronic Science and Technology of China (UESTC), Chengdu, China, in 2000, 2003, and 2009, respectively. He is currently an Associate Professor with the School of Information and Communication Engineering, UESTC. His research interests include multi-input multi-output (MIMO) radar, cognitive radar, array signal processing, and space-time adaptive processing.

**Zishu He** (Senior Member, IEEE) was born in Sichuan, China, in 1962. He received the B.S., M.S., and Ph.D. degrees in signal and information processing from the University of Electronic Science and Technology of China (UESTC), in 1984, 1988, and 2000, respectively. He is currently a Professor in signal and information processing with the School of Information and Communication Engineering, UESTC. His research interests include array signal processing, space-time adaptive processing, digital beam forming, the theory of multiple-input multiple-output (MIMO) communication and MIMO radar, and interference cancellation.